



HAL
open science

Illumination of a progressive allosteric mechanism mediating the glycine receptor activation

Sophie Shi, Solène N Lefebvre, Laurie Peverini, Adrien Cerdan, Paula Milán Rodríguez, Marc Gielen, Jean-Pierre Changeux, Marco Cecchini, Pierre-Jean Corringer

► To cite this version:

Sophie Shi, Solène N Lefebvre, Laurie Peverini, Adrien Cerdan, Paula Milán Rodríguez, et al.. Illumination of a progressive allosteric mechanism mediating the glycine receptor activation. *Nature Communications*, 2023, 14 (1), pp.795. 10.1038/s41467-023-36471-7 . pasteur-03993599v1

HAL Id: pasteur-03993599

<https://pasteur.hal.science/pasteur-03993599v1>

Submitted on 17 Feb 2023 (v1), last revised 17 Feb 2023 (v2)

HAL is a multi-disciplinary open access archive for the deposit and dissemination of scientific research documents, whether they are published or not. The documents may come from teaching and research institutions in France or abroad, or from public or private research centers.

L'archive ouverte pluridisciplinaire **HAL**, est destinée au dépôt et à la diffusion de documents scientifiques de niveau recherche, publiés ou non, émanant des établissements d'enseignement et de recherche français ou étrangers, des laboratoires publics ou privés.



Distributed under a Creative Commons Attribution 4.0 International License

1 **Illumination of a progressive allosteric mechanism mediating the glycine**
2 **receptor activation**

3

4 Sophie Shi^{1,2#}, Solène N Lefebvre^{1,2#}, Laurie Peverini^{1§}, Adrien Cerdan^{4§}, Paula Milán
5 Rodríguez⁴, Marc Gielen^{1,3}, Jean-Pierre Changeux⁵, Marco Cecchini^{4*}, Pierre-Jean Corringer^{1*}

6

7 1 Institut Pasteur, Université de Paris, CNRS UMR 3571, Channel-Receptors Unit, Paris,
8 France

9 2 Sorbonne Université, Collège doctoral, Paris, France

10 3 Sorbonne Université, 21 rue de l'École de Médecine, 75006 Paris, France.

11 4 Institut de Chimie de Strasbourg, UMR7177, CNRS, Université de Strasbourg, F-67083
12 Strasbourg Cedex, France

13 5 Neuroscience Department, Institut Pasteur, Collège de France, Paris, France

14

15 # equal contribution

16 § equal contribution

17 *Corresponding authors

18 Email:

19 mcecchini@unistra.fr

20 pierre-jean.corringer@pasteur.fr

21

22 **Abstract**

23 Pentameric ligand-gated ion channel mediate signal transduction at chemical synapses by
24 transiting between resting and open states upon neurotransmitter binding. Here, we investigate
25 the gating mechanism of the glycine receptor fluorescently labeled at the extracellular-
26 transmembrane interface by voltage-clamp fluorimetry (VCF). Fluorescence reports a glycine-
27 elicited conformational change that precedes pore opening. Low concentrations of glycine,
28 partial agonists or specific mixtures of glycine and strychnine trigger the full fluorescence signal
29 while weakly activating the channel. Molecular dynamic simulations of a partial agonist bound-
30 closed Cryo-EM structure show a highly dynamic nature: a marked structural flexibility at both
31 the extracellular-transmembrane interface and the orthosteric site, generating docking
32 properties that recapitulate VCF data. This work thus illuminates a progressive propagating
33 transition towards channel opening, displaying structural plasticity with novel implications
34 concerning the mechanism of action of allosteric effectors.

35 **Introduction**

36 Pentameric ligand-gated ion channels (pLGICs), including nAChRs, 5-HT₃Rs, GlyRs and
37 GABA_ARs constitute a superfamily of transmembrane receptors mediating intercellular
38 communications in the nervous system^{1,2}. They transduce the binding of a neurotransmitter
39 at their orthosteric site into the opening of an intrinsic ion channel, leading to ion fluxes that
40 promote cell excitation or inhibition. The orthosteric binding site also binds partial agonists,
41 with less efficacy than full agonists to elicit channel opening, and competitive antagonists.
42 These distinct pharmacological profiles were interpreted in terms of the concerted two-state
43 model (Monod et al., 1965) based upon a pre-existing equilibrium between the resting and
44 active states that is differentially shifted depending on the nature of the effector³⁻⁵.

45 In between these two equilibrium states, the conformational pathway that the protein follows
46 during activation remains elusive. Single-channel recordings of numerous mutants of the
47 muscle nAChR analyzed by REFERs (rate equilibrium linear free energy relationships)
48 suggested an early motion of the extracellular domain (ECD) and a late motion of the
49 transmembrane domain (TMD) during activation⁶. Likewise, single-channel kinetics analysis
50 on GlyRs and nAChRs were interpreted via a model involving a multistep process since
51 accurate fitting of the experimental data require the introduction of intermediate states “flip”⁷
52 or “primed”⁸ in the gating transition. Although capturing structural reorganizations only
53 indirectly, the electrophysiological data suggest that the transition is progressive, with the
54 conformational changes starting from the ECD where the orthosteric site is located and
55 propagating to the TMD to reach the channel gate. Moreover, computational studies of various
56 pLGICs by Molecular Dynamics highlight their passage through a complex conformational
57 landscape with the gating transition being composed of a progressive reorganization of the
58 multimeric receptor architecture⁹⁻¹³.

59 At the structural level, fluorescence experiments provided evidence that the bacterial pLGIC
60 homologue GLIC undergoes a progressive reorganization, with a first pre-activation step
61 involving a quaternary compaction of the ECD¹⁴ followed by pore opening associated with a
62 structural reorganization of the TMD and ECD-TMD interface¹⁵. However, direct evidence for
63 a progressive signal transduction in eukaryotic receptors is essentially lacking, despite recent
64 cryo-EM structures of pLGICs revealing that the binding of orthosteric ligands is often
65 accompanied by a significant reorganization of the extracellular domain (ECD), while the
66 channel remains closed at the transmembrane domain (TMD), e.g. in 5-HT₃R^{16,17}, GABA_AR
67¹⁸, GlyR¹⁹ and nAChR²⁰. Thus, pLGIC structures appear to be more flexible than previously
68 anticipated, suggesting that ligands or classes of molecules could stabilize specific
69 conformation(s) in the conformational landscape accessible to the protein. Whether the
70 captured conformations solved by cryo-EM correspond or not to intermediates during
71 transitions on the pathway to channel activation remains an open question. Addressing these

72 questions requires monitoring the conformational dynamics of a fully functional receptor
73 embedded in a plasma membrane and probing its relationship with both activation and
74 desensitization. The Voltage-Clamp Fluorimetry (VCF) technique is perfectly suited to this
75 purpose, since it allows the simultaneous recording of local conformational changes by
76 fluorescence together with transmembrane current fluxes by electrophysiology.

77 Here, we used the $\alpha 1$ homomeric GlyR, which is surely among the best characterized pLGIC
78 by electrophysiology^{21,22}, cryo-EM alone or in complex with ligands^{19,16,23}, VCF²⁴⁻³¹, and MD
79 simulations^{32,33}. We report the development and characterization of a mutant GlyR $\alpha 1$ bearing
80 a fluorescent sensor at the interface between ECD and TMD. Its pharmacological
81 characterization using different allosteric effectors by VCF coupled to MD simulations and
82 docking illuminates the occurrence of intermediates, displaying dynamic properties of the ECD,
83 on the path to channel opening consistent with a progressive mechanism of gating.

84

85 **Results**

86 ***Design of a fluorescent-quenching sensor reporting conformational changes at the*** 87 ***ECD-TMD interface***

88 To generate a fluorescent sensor related to the activation process, we compared the structure
89 of the zebrafish GlyR $\alpha 1$ in the resting-like apo state (PDB:6PXD) with the glycine-bound open-
90 channel structure (PDB:6PM6)¹⁹. Beside the well documented contraction of the orthosteric
91 site at the subunit-subunit interfaces in the ECD and the opening of the channel in the TMD,
92 visual inspection also shows an expansion of the ECD-TMD interface, where the Cys-loop of
93 each subunit moves away by nearly 3 Å from the pre-M1 region of the adjacent subunit (Fig.
94 1A, B). In order to monitor this reorganization, we used the tryptophan quenching technique
95 that can sense the relative place of two residues^{34,35}. This technique is particularly relevant to
96 monitor distance changes of 5-15 Å range^{14,15}. We introduced a cysteine at position Q219 in
97 the pre-M1 region previously used for labeling with fluorescent dyes²⁸, together with a
98 tryptophan in Cys-loop at position K143, in order to quench the fluorophore in a conformation
99 dependent manner (Fig. 1A, B).

100

101 ***The quenching sensor K143W/Q219C reveals glycine-elicited fluorescence variations at*** 102 ***much lower glycine concentrations than currents***

103 The endogenous extracellular single cysteine of the human GlyR $\alpha 1$ was mutated to avoid non-
104 specific labeling, yielding WT-C41V displaying wild-type like properties in electrophysiology
105 (Supplementary Fig. 1). All mutations show here present this background C41V mutation.
106 Upon introduction of the quenching sensor mutations, the unlabeled K143W/Q219C was
107 analyzed by two-electrode voltage clamp electrophysiology (TEVC). In all dose-response
108 curves presented here, we used a brief perfusion (10-30 seconds) of the glycine solutions to

109 reach a current plateau with no apparent desensitization. The unlabeled K143W/Q219C
110 displays an $EC_{50}^{current}$ that is 16-fold higher than that of WT-C41V (Supplementary Fig. 3A, B,
111 Table 1), indicating a loss-of-function phenotype. We controlled that the mutations do not
112 impair ion channel permeation by performing outside-out single-channel recordings (Fig. 2C)
113 and measuring a unitary conductance of 86.7 ± 4.6 pS that is identical to that of WT-C41V
114 (85.7 ± 4.5 pS) (Supplementary Fig. 1).

115 After labeling with MTS-TAMRA (Figure 1A), K143W/Q219C was analyzed by VCF, using a
116 dedicated recording chamber (Supplementary Fig. 2). Its $EC_{50}^{current}$ decreases by 1.6-fold,
117 indicating that the labeling produces a slight gain-of-function that partially counterbalances the
118 effect of the K143W/Q219C mutations. Robust glycine-elicited fluorescence variations were
119 also observed (Fig. 2A, B). They start at non-activating glycine concentrations (5-25 μ M) and
120 reach a plateau at the beginning of the current dose-response curve, with a maximal
121 fluorescence amplitude $\Delta F/F$ corresponding to a 12.9 ± 1.0 % decrease. Therefore, the EC_{50}^{fluo}
122 is 73-fold lower than the $EC_{50}^{current}$. As a control, we also recorded the labeled Q219C/K143F
123 and Q219C, that show weak $\Delta F/F$ (no variation and a 2 ± 0.2 % decrease, respectively)
124 (Supplementary Fig. 3B, C), indicating that the $\Delta F/F$ of the K143W/Q219C sensor is dominated
125 by the quenching provided by the introduced tryptophan. Of note, the MTS-TAMRA used here
126 corresponds to a commercial mixture of isomers (Fig. 1A), each of which was verified to
127 produce the same VCF pattern separately (Supplementary Fig. 3D).

128

129 ***The quenching sensor K143W/Q219C reports an “intermediate” conformational*** 130 ***reorganization occurring before the onset of currents***

131 Inspection of the current/fluorescence time courses and quantification by single exponential
132 fitting reveals important features. First, the onset of both the fluorescence and current traces
133 is faster with increased glycine concentrations whereas their offset during agonist rinsing is
134 slower (Fig. 2D, F, Supplementary Table 3, Supplementary Fig. 4). Second, at each glycine
135 concentration, the rise time of the fluorescence change is systematically faster than that of the
136 currents whereas the offset tends to be slower particularly at glycine concentrations >200 μ M.
137 It is noteworthy that these kinetic values are limited by the rate of agonist perfusion in the
138 recording chamber, and do not reflect the intrinsic kinetics of the receptor. For instance, upon
139 perfusion of 200 μ M Gly (Fig. 2D), the glycine concentration at the oocyte surface will
140 progressively rise, first reaching the concentration eliciting full fluorescence variation (100 μ M),
141 then reaching after a delay the concentration eliciting currents (200 μ M). Conversely, upon
142 glycine washing, its concentration will rapidly drop below 100 μ M, causing deactivation, but
143 will take more time to drop below the concentrations causing fluorescence variations. The
144 relatively slow kinetics of perfusion of the agonist thus separate in time the molecular events
145 causing the fluorescence variation and the current, the former preceding the later.

146 Fig. 2A, B shows that 100 μ M glycine, at steady state, elicits most of the fluorescence variation
147 but no significant current. This indicates that the receptor has completed the full movement
148 reported by the quenching sensor with a closed channel. Hence, VCF data provide direct
149 evidence for a structural conformational transition toward one or a cluster of conformations that
150 are structurally distinct from both resting and active. Importantly, kinetic data show that these
151 conformations appear before channel opening in our recording conditions (Fig. 2D, F). This
152 suggests that they correspond to early “intermediate conformation(s)” along the allosteric
153 transition pathway to activation that are not related to desensitization. To further investigate
154 this possibility, we applied glycine at high concentration (30 mM) for a prolonged period (1
155 min), leading to a rapid onset of the current followed by a slower decrease (34.6 ± 4.9 %
156 decrease after 1 min) caused by desensitization. The fluorescence strongly decreases during
157 the activation phase, then reaches a plateau and remains stable during the second phase,
158 providing evidence that the quenching sensor does not report movements related to
159 desensitization (Fig. 2E).

160

161 ***The Gly-elicited fluorescent and current changes are linked to glycine binding to the*** 162 ***orthosteric site***

163 The marked separation of the current (ΔI) and fluorescence (ΔF) dose-response curves raises
164 the possibility that both processes could be mediated by different classes of glycine binding
165 sites within and outside the orthosteric site. To challenge this possibility, we introduced two
166 mutations into the orthosteric binding site (N61D/N46D, Fig. 3A) that strongly decrease the
167 affinity for glycine³⁶. The K143W/Q219C/N61D/N46D shows a parallel rightward shift of both
168 ΔI and ΔF curves (15-fold and 68-fold increase in EC_{50}^{current} and EC_{50}^{fluo} , respectively) (Fig. 3B,
169 C, Table 1), indicating that both processes are strongly linked to glycine binding to the
170 orthosteric site. We also found that ΔF changes are sensitive to known allosteric hyperekplexia
171 mutations at the ECD-TMD interface. Combined with K143W/Q219C, the loss of function
172 R219Q³⁷, located at the top of the M2 helix, fails to generate currents (certainly due to the
173 combination with K143W) but a ΔF is observed and its curve is shifted to higher glycine
174 concentrations (Supplementary Fig. 5A). Conversely, combined with K143W/Q219C, the gain
175 of function V280M³⁸, located within the loop linking the M2 and M3 helices (M2-M3 loop) does
176 not show fluorescence variation, but currents with a ΔI curve shifted to lower concentrations.
177 In addition, it shows high leak currents in the absence of glycine that are inhibited by
178 strychnine, indicating constitutive channel openings (Supplementary Fig. 5B, C).

179

180

181 ***Partial agonists, strychnine and propofol differentially affect the current and*** 182 ***fluorescence variations***

183 First, we investigated the effect of agonists that bind at the orthosteric site but are less effective
184 than glycine at activating the receptor, i.e., partial agonists. We selected β -alanine and taurine.
185 They trigger respectively 54-98% and 20-42% of the glycine-elicited maximum current³⁹⁻⁴¹ in
186 TEVC^{39,42,43,41}. On K143W/Q219C, we found that their efficacy decreases, eliciting only $6.1 \pm$
187 2.2% and $2.0 \pm 1.4\%$ of the glycine-elicited maximum current respectively (Fig. 4A, B). Such
188 a decrease in efficacy is commonly observed for loss-of-function mutants³¹. Surprisingly, both
189 partial agonists elicit the full fluorescence variation recorded with glycine. β -Alanine and taurine
190 show a large difference in the ΔF and ΔI dose-response curve, their EC_{50}^{fluo} being respectively
191 66- and 70-fold lower than their $EC_{50}^{current}$ (Table 1). β -Alanine and taurine thus trigger the full
192 transition mediating the fluorescence change, but they are weakly effective to trigger the
193 “downward” process of channel opening.

194 Next, we investigated the competitive antagonist strychnine. When strychnine is applied alone
195 at $5\ \mu M$, no current is observed as expected, but the fluorescence increases over the baseline
196 in a direction opposite to the glycine-elicited quenching (dequenching). It then reaches a
197 plateau corresponding to $38 \pm 6\%$ in absolute amplitude of the maximal glycine elicited
198 fluorescence variation. We then applied strychnine ($5\ \mu M$) during a perfusion of glycine at
199 different concentrations (Fig. 5). At $100\ \mu M$ glycine, strychnine inhibits both the current and
200 fluorescence variations elicited by glycine. As before, strychnine tends to increase the
201 fluorescence over the baseline, but the effect is not significant. At $1\ mM$ of glycine, strychnine
202 still totally inhibits the current, but surprisingly the glycine-elicited fluorescence quenching is
203 decreased by only $48 \pm 4\%$. Finally, at $10\ mM$ of glycine, strychnine inhibits only $77 \pm 2\%$ of
204 the current, while the fluorescence is almost not affected. Therefore, co-application of
205 strychnine with various concentrations of glycine differentially affects the fluorescence
206 variations and currents.

207 Last, we investigated the general anesthetic propofol, a positive allosteric modulator of GlyR $\alpha 1$
208 that binds in the TMD of pLGICs⁴⁴⁻⁴⁷. At 200 and $300\ \mu M$, propofol alone elicits a fluorescence
209 variation of about 3-5% $\Delta F/F$ without activating the receptor, while at higher concentrations it
210 also activates the currents in the absence of glycine (Supplementary Fig. 6). At a lower 100
211 μM concentration, propofol alone does not elicit significant ΔF . Interestingly, co-application of
212 propofol with a range of glycine concentrations shows that it potentiates by $21 \pm 7\%$ the
213 maximal currents and shifts by 8-fold the ΔI curve to lower concentrations. In contrast, propofol
214 does not affect significantly the ΔF curve (Fig. 4C, Supplementary Table 1). Propofol thus does
215 not alter the transition mediating the fluorescence change, but specifically facilitates the
216 “downward” process of channel opening.

217 In conclusion, various pharmacological conditions yield a common phenotype with a change
218 in ΔF with comparatively weaker or no change in ΔI : they are low glycine concentrations, partial
219 agonists, specific mixtures of glycine and strychnine and $200-400\ \mu M$ of propofol alone. This

220 phenotype suggests that a substantial fraction of the receptors has undergone the local
221 conformational motion causing quenching of K143W/Q219C in the lower part of the ECD but
222 with a closed channel. However, it is possible that the glycine-strychnine combination and
223 propofol alone change the environment of the sensor in a similar way as partial agonists and
224 agonists do, giving similar ΔF signature, while the rest of the ECD could present different
225 conformations. This is especially possible for propofol alone as it binds to the TMD of GlyRs
226 and might thus present an alternative mechanism.

227

228 ***The R271C mutant also shows a relative increased fluorescence variation when***
229 ***activated by taurine as compared to glycine.***

230 Among pLGICs, the GlyR has been extensively studied by VCF by the team of Lynch *et al*,
231 with labeling of the upper M2 helix at position R271^{25,31}, the orthosteric site, the loop 2 and
232 pre-M1 regions^{28,30}, and the TMD^{26,27}. In all cases, the fluorescence dose-response curves
233 were superimposed or right-shifted as compared to the current dose-response curve under
234 glycine application (Supplementary Fig. 7). Thus, the leftward shift of the ΔF dose-response
235 curve shown here seems unique.

236 However, another landmark of K143W/Q219C concerns the action of partial agonists, that
237 produce much higher maximal $\Delta F/\Delta I$ ratios than glycine. Interestingly, R271C³¹ was also
238 reported to display such a phenotype with taurine. On our VCF setup, with glycine, R271C
239 produces an 18-fold shift of the ΔI curve to higher concentrations as compared to WT, and a
240 near superimposition of the ΔI and ΔF curves. Taurine at saturation elicits significantly higher
241 ΔF than ΔI , respectively $21 \pm 3.4\%$ and $5.4 \pm 2.3\%$ of glycine values. In addition, for taurine,
242 the ΔF curve is shifted by 2-fold to lower concentrations as compared to the ΔI curve (Fig. 6A,
243 B). These data, that are in qualitative agreement with those of Pless *et al.* (2007), indicate that
244 a fraction of the taurine-elicited states of R271C present a fluorescence variation with a closed
245 channel.

246

247 ***Molecular dynamics simulations of a cryo-EM partial-agonist bound state recapitulates***
248 ***the pharmacological profile of the intermediate state(s)***

249 A recent cryo-EM analysis of the zebrafish GlyR¹⁹ has revealed that the partial agonists taurine
250 and GABA may stabilize a previously unseen closed-channel state (referred to as "tau-closed")
251 characterized by a significant reorganization of the ECD compared to the apo-state. We
252 hypothesized that the intermediate conformation(s) illuminated by VCF is structurally similar to
253 tau-closed. To explore this hypothesis, we carried out all-atom MD simulations of the zebrafish
254 apo-closed (PDB:6PXD), tau-closed (PDB:6PM3) and tau-open (PDB:6PM2) structures
255 embedded in a POPC bilayer. In addition, since strychnine nicely fits the orthosteric site of

256 apo-closed, we performed MD simulations of the strychnine-closed (stry-closed) complex as
257 well. For each system, five independent simulations of 100 ns were carried out.

258 The structural stability of the protein was analyzed by monitoring the root-mean-square
259 fluctuations (RMSF) from the average structure extracted from MD (Fig. 7A). In addition, we
260 calculated the evolution of the twisting and blooming angles of the ECD during each simulation
261 (Supplementary Fig. 8, Supplementary Table 4). The simulations show that: i. apo-closed is
262 the most flexible conformational state of the receptor (Fig. 7A) and strychnine binding stabilizes
263 the bloomed conformation (expended ECD as seen in the Apo-closed cryo-EM structure),
264 rigidifying the ECD; ii. the ECD of tau-closed is remarkably more flexible than that in tau-open
265 despite the apparent structural similarity in the cryo-EM coordinates that show an un-bloomed
266 (compaction of the ECDs) structure; iii. tau-closed has a weaker affinity for taurine than tau-
267 open as evidenced by four spontaneous unbinding events in the tau-closed simulations, that
268 are associated with significant blooming of the structure (Supplementary Fig. 10); iv. the C-
269 loop that is critical for orthosteric ligand binding is more flexible in tau-closed (RMSF of 3.5 Å)
270 than in tau-open (RMSF of 2.5 Å) or stry-closed (RMSF of 2.0Å); v. the conformational
271 dynamics of the ECD-TMD interface (i.e., β 1- β 2 loop, Cys-loop, and the β 8- β 9 loop) is
272 enhanced in tau-closed relative to apo-closed and tau-open. Taken together, the simulation
273 results highlight that the tau-closed conformation features a surprising dynamic character,
274 which is remarkably different from that of tau-open and apo-closed and could not be deduced
275 from the comparison of static cryo-EM structures only.

276 To explore the correlation between MD and VCF data, we quantified the reorganization of the
277 fluorescence quenching sensor, as well as the binding of strychnine.

278 First, we calculated the average distance between the C α carbons of the VCF quenching
279 sensor (corresponding to K143W/Q219C). It is 13.0 ± 0.7 Å in stry-closed and apo-closed and
280 this value increases to 14.7 ± 1.4 Å and 16.4 ± 1.0 Å in tau-closed and tau-open, respectively.
281 Therefore, the significant reorganization seen in the simulations of the sensor from the apo to
282 the tau-closed conformation is compatible with a change in fluorescence during this transition.
283 We speculate that, during the separation of the C α carbons, the rather long and flexible TAMRA
284 “side chain” anchored at C219 reorganizes to interact more frequently with W143, generating
285 fluorescence quenching.

286 Second, the binding of strychnine to the various conformations of GlyR was explored by
287 docking. As expected, favorable docking scores were obtained in stry-closed (-12.1 kcal/mol)
288 and apo-closed (-10.3 kcal/mol) from cryo-EM. By contrast, both tau-open and tau-closed from
289 cryo-EM feature an orthosteric site that is too small to accommodate strychnine and the
290 docking scores were largely unfavorable. To account for the intrinsic flexibility of the protein,
291 the docking experiments were repeated using protein conformations extracted from the MD
292 trajectories. Assuming that a docking experiment was successful when the docking score was

293 < -9.3 kcal/mol (i.e. within 10% of the score obtained in stry-closed), the success rate for
294 docking strychnine was determined by counting the fraction of successful docking over 500
295 protein snapshots from MD of apo-closed, tau-closed, and tau-open. As shown in Fig. 7B,
296 docking of strychnine was successful at 26% (std dev 6.5%) in apo-closed, 6.6% (std dev
297 7.0%) and with large deviations among replicas in tau-closed, and only 2.2% (std dev 1.4%) in
298 tau-open. We conclude that the enhanced flexibility of the tau-closed structure makes it very
299 different from tau-open and compatible with strychnine binding.

300 Although this analysis was carried out on the WT zebrafish receptor, we performed
301 control MD simulations of the K143W/Q219C/C41V triple mutant in the tau-open and tau-
302 closed states, giving similar results (Supplementary Fig. 9). The simulation results support the
303 conclusion that the intermediate conformation(s) revealed by VCF, concerning both (partial)
304 agonists and glycine-strychnine combinations, is consistent with a highly dynamic cluster of
305 states as described by MD simulation started from the cryo-EM tau-closed structure.

306

307 **Discussion**

308 The VCF data on K143W/Q219C provide structural evidence for an early intermediate step in
309 the global activation path of GlyR. Indeed, upon glycine application, they reveal the emergence
310 of one or more intermediate conformation(s) characterized by a change in fluorescence but no
311 current, followed by channel opening with no further change in fluorescence. Two lines of
312 evidence support that the intermediate conformation(s) illuminated by VCF is on-path to the
313 global activation process: i. Receptors in this intermediate conformation(s) are activatable
314 since they appear before the onset of the currents, and are thus not desensitized, ii. Receptors
315 in the intermediate conformation(s) are stabilized by partial agonists, low glycine
316 concentrations, and mixtures of glycine and strychnine, showing a pharmacological profile “in
317 between” those stabilizing the resting and active states.

318

319 It is noteworthy that the mutations introduced here to anchor the fluorescence quenching
320 sensor (K143W/Q219C) cause an 8-fold increase in $EC_{50}^{current}$ of glycine, and a decreased
321 efficacy of the partial agonists to activate the receptor, yet with an intact conductance of the
322 channel. This indicates a destabilization of the active state. Concerning fluorescence, the ΔF
323 curve displays higher sensitivity than the ΔI curve, indicating that partial binding of glycine is
324 sufficient to trigger the resting to intermediate(s) conformational transition. In addition,
325 strychnine alone produces a fluorescence variation in opposite direction to agonists,
326 suggesting that the intermediate(s) conformation(s) are already substantially populated in the
327 absence of ligand, with strychnine shifting the spontaneous equilibrium back toward the resting
328 state⁴⁸. For partial agonists, they even mainly stabilize the intermediate(s) conformation at
329 saturation, with a very minor representation of the active state.

330 Interestingly, we found that a non-activating concentration of propofol potentiates the currents
331 without change of the ΔF curve, suggesting a specific action of propofol on the intermediate(s)
332 to active transition. We also report that the gain of function mutant V280M does not show
333 fluorescence changes. We suggest that this mutant could be populated mainly in the intermediate(s)
334 state in the absence of agonist.

335

336 An important observation from VCF is that taurine binding stabilizes primarily the intermediate
337 state(s). The structure of the “tau-closed” state of the zebrafish GlyR recently solved by cryo-
338 EM is a strong candidate for an early on-pathway intermediate during the global activation
339 process¹⁹. However, docking experiments show that this structure is unable to accommodate
340 the bulky antagonist strychnine, a feature that is inconsistent with our VCF data. Interestingly,
341 MD simulations of the tau-closed structure provide a way to explain this discrepancy. In fact,
342 the simulations reveal that the ECD is surprisingly dynamic in the tau-closed state and samples
343 the spontaneous opening of the orthosteric site on the sub- μ s time scale, which makes it
344 compatible with strychnine binding. Combined with the VCF data, these observations suggest
345 that receptors in the presence of mixtures of strychnine and agonists would keep an overall
346 intermediate-like conformation with significant asymmetry at the ECD and at the orthosteric
347 sites. Some sites would bind agonists/partial agonists in an active-like compact state, while
348 others would bind strychnine in a resting-like expanded state. We speculate that the same
349 mechanism applies in the case of partial occupation of the orthosteric sites by glycine,
350 accounting for a maximal fluorescence variation at low glycine concentration with little current,
351 which explains the large separation of the ΔI and ΔF dose-response curves.

352 The simulations reveal that the tau-closed state presents a unique dynamic personality that is
353 remarkably different from those at the resting and active states. In fact, comparison of the
354 atomic fluctuations in the different conformations reveals that the flexibility of the ECD-TMD
355 interface is surprisingly enhanced in tau-closed relative to both apo-closed (resting-like) and
356 tau-open (active-like). We speculate that the unique dynamic signature of tau-closed originates
357 from the hybrid nature of this state, which features an ECD in a nearly active conformation
358 along with a resting-like TMD endowed with a closed channel. This apparent mismatch at the
359 ECD-TMD interface, which enhances the flexibility of the ECD domain and its blooming in tau-
360 closed, favors the structural plasticity for promiscuous orthosteric-ligand binding. This
361 hypothesis is consistent with the large re-organization of the pre-M1 and Cys-loop regions
362 probed by VCF in the absence of currents and suggests that the tau-closed structure and its
363 dynamic character provide a reasonable representation of the early intermediate
364 conformations found not only with partial agonists, but also with glycine at sub-saturation or
365 with glycine and strychnine mixtures.

366 From combined VCF and MD data, we thus propose a speculative model of receptor activation
367 depicted in Figure 8, where the receptor transits through a cluster of highly dynamic
368 intermediate conformations, allowing significant local asymmetry at the level of the orthosteric
369 site (and also potentially in the upper ECD), but a more symmetric organization at the ECD-
370 TMD interface where the fluorescent sensors are anchored. Although we cannot exclude the
371 existence of alternative intermediate states in different pharmacological conditions e.g.
372 involving changes in the local environment of the fluorescence sensors, the MD simulations of
373 the cryo-EM Tau-closed state provides a reasonable and unifying explanation of the
374 intermediate states recorded with (partial) agonists and the glycine-strychnine mixture.

375

376 Our data also suggest that a fraction of R271C receptors, when activated by taurine, display
377 an intermediate-like conformation. It is noteworthy that R271C and K143W/Q219C cause a
378 similar 10-fold increase in $EC_{50}^{current}$ of glycine (Supplementary Fig. 7). We thus speculate that
379 their major difference relies on the resting to intermediate equilibrium, which is strongly shifted
380 toward the intermediate(s) in K143W/Q219C and much less in R271C. Interestingly,
381 K143W/Q219C and R271C are located at both extremities of the M2-M3 loop which undergoes
382 a large outward movement during gating (Fig. 6A).

383 Concerning the WT zebrafish GlyR studied by cryo-EM, literature data suggest a contribution
384 of around 7% of Tau-closed states at taurine saturation¹⁹. It is thus likely that, in the WT human
385 GlyR context, intermediate(s) state would also be sparsely populated in the presence of partial
386 agonists. We speculate that the K143W mutation, strongly stabilizes the intermediate(s)
387 conformation, this allowing its robust monitoring by VCF. In retrospect, this might explain why
388 the “intermediate” phenotype has rarely been observed in the previous VCF studies of the
389 GlyR. Of note, previous single-channel works on nAChRs and GlyRs suggested the
390 contribution of flipped/primed intermediate states on receptor’s activation. Flipped/primed are
391 incompletely stabilized by partial agonists, underlying their limited efficacy to fully activate the
392 receptor^{8,49}. This is in contrast with the intermediate conformation(s) unraveled here, which is
393 fully stabilized by partial agonists and consequently must occur earlier than the flip/prime
394 transition.

395

396 Phenotypes resembling the one presented here have been already described for the bacterial
397 channel GLIC and cationic pLGICs. With GLIC, we reported a “pre-activation” phenotype for a
398 series of quenching sensors at the ECD interface and M2-M3 loop^{14,15}. They all report
399 fluorescence variations at non-activating agonist (proton) concentrations and the fluorescence
400 variation was faster (ms range measured by stopped-flow) than the onset of activation (10-100

401 of ms measured by patch-clamp)⁵⁰. It is noteworthy that M2-M3 loop is located just in between
402 the quencher (W143) and the fluorophore (C219) in the GlyR structure (Figure 1).
403 In case of cationic pLGICs using VCF, labeling of the muscle nAChR ($\alpha\gamma\alpha\delta\beta$ subtype) at the
404 top of TMD (position 19' located at the upper end of M2 helix and facing the ECD) reports a
405 100-fold lower EC_{50}^{fluo} as compared to $EC_{50}^{current}$ for ACh (binding the $\alpha\delta$ interface), while no
406 difference was observed for epibatidine (binding the $\alpha\gamma$ interface). Moreover, the change in
407 fluorescence occurs with fast kinetics and pharmacological considerations support the
408 occurrence of a conformational transition toward a singly liganded closed-channel state⁵¹.
409 Labeling at the 19' position has also been performed on the 5-HT₃R, consistent with monitoring
410 a pre-active reorganization¹⁷. Finally, labeling of the $\alpha 4\beta 4$ receptor in the extracellular loop 5
411 of $\alpha 4$ shows a 5-fold lower EC_{50}^{fluo} as compared to $EC_{50}^{current}$ for ACh suggesting that loop 5
412 moves before channel activation. Additionally, the antagonist DH β E elicits also a robust
413 fluorescent change⁵² which suggests a highly dynamic nature of loop 5 in the activation and
414 inhibition process. Altogether, data on the GlyR, GLIC and possibly nAChR/5HT₃R provide
415 evidence for intermediate transitions involving structural reorganizations mainly at the ECD
416 and/or ECD-TMD interface. This idea is in line with REFERs analysis of the muscle nAChR,
417 that suggests that the orthosteric site and M2-M3 loop move very early during the activation
418 transition⁶. It is also consistent with simulations describing the gating isomerization in terms
419 of a combination of two consecutive quaternary transitions named twisting and blooming². In
420 this view, the intermediate conformation(s) illuminated by VCF would correspond to the
421 completion of the un-blooming isomerization (i.e., compaction of the ECD) in a still closed-
422 channel receptor. The apparent absence of significant twisting during GlyR activation (Figure
423 S7) and its role on gating remain to be understood. Altogether, while the detailed activation
424 mechanism may differ between different pLGIC subtypes, the collected data highlight a general
425 activation mechanism in pLGICs characterized by a progressive conformational propagation
426 from the ECD to the TMD.

427

428 In conclusion, this work illustrates the interest of combining VCF and MD approaches to identify
429 functional intermediate conformations, characterize their flexibility, and annotate Cryo-EM
430 structures to functional states. Noteworthy, such intermediate conformations may contribute to
431 signal transduction in the postsynaptic membrane. The progressive transition also illuminates
432 the mode of action of allosteric effectors and may be valuable for drug-design purposes.

433

434 **Materials and methods:**

435 ***Site-directed mutagenesis***

436 The gene coding the full-length human glycine α 1-subunit was cloned into the pMT3 plasmid
437 containing an Ampicillin resistance gene. The PCR reaction was done with CloneAmp Hifi
438 premix from Takara.

439

440 ***α 1 homomeric glycine receptor expression in oocytes***

441 *Xenopus Laevis* oocytes at stage VI are ordered from Portsmouth European *Xenopus* resource
442 center and Ecocyte Biosciences and kept in Barth's solution (87.34 mM NaCl, 1 mM KCl, 0.66
443 mM CaNO₃, 0.72 mM CaCl₂, 0.82 mM MgSO₄; 2.4 mM NaHCO₃, 10 mM HEPES and pH
444 adjusted at 7.6 with NaOH). Ovary fragments obtained from Portsmouth European *Xenopus*
445 resource center are treated as previously described⁵³. cDNA coding the α 1-subunit at 80 ng/ μ L
446 is co-injected with a cDNA coding for GFP at 25 ng/ μ L into the oocyte nucleus by air injection.
447 The injection pipettes are done with the capillary pipette (Nanoject II, Drummond) and PC-10
448 dual stage glass micropipette puller. Injected oocytes are incubated at 18°C for 3-4 days for
449 expression.

450

451 ***Labeling of the cysteine***

452 MTS-TAMRA and MTSR (Clinisciences) is dissolved in DMSO to obtain a final stock
453 concentration of 10 mM and conserved at -20 °C. For labeling, oocytes expressing the
454 receptors are incubated in 10 μ M MTS-TAMRA (diluted in Barth's solution to obtain a final
455 DMSO concentration of 0.1%) at 16-18 °C for 20 mins before the recording. The procedure is
456 similar for other fluorescent dyes (MTS-5-TAMRA, MTS-6-TAMRA). For MTSR, oocytes are
457 incubated in 10 μ M MTSR at 16-18°C for less than 1 min.

458

459 ***Two electrode voltage-clamp on oocytes***

460 Oocytes expressing GlyR constructs are recorded in ND96 solution (96 mM NaCl, 2 mM KCl,
461 5 mM HEPES, 1 mM MgCl₂, 1.8 mM CaCl₂ and pH adjusted at 7.6 with NaOH). Molecules that
462 are not 100% soluble in aqueous solution are first dissolved in DMSO and then diluted in ND96
463 to have a DMSO final concentration < 0.1 %. Currents were recorded by a Warner OC-725C
464 amplifier and digitized by Digidata 1550A and Clampex 10 (Molecular Devices). Currents were
465 sampled at 500 Hz and filtered at 100 Hz. The voltage clamp is maintained at -60 mV at room
466 temperature. Recording pipettes were made with Borosilicate glass with filament (BF150-110-
467 7.5, WPI) with a PC-10 dual stage glass micropipette puller to obtain pipettes of resistances
468 comprised between 0.2 and 2 M Ω .

469

470 ***Voltage-Clamp Fluorometry on oocytes***

471 Injected oocytes are placed on a home-designed chamber with the animal pole turning toward
472 the microscope objective. Currents were recorded by GeneClamp 500 voltage patch clamp

473 amplifier (Axon instruments) and digitized by Axon Digidata 1400A digitizer and Clampex 10.6
474 software (Molecular Devices). TAMRA excitation is done by illumination with a 550 nm LED
475 (pE-4000 CoolLED, 15%-20% intensity) through a FF01-543_22 bandpass filter (Semrock).
476 The fluorescence emission goes through a FF01-593_40 bandpass filter (Semrock) and is
477 collected by a photo-multiplier H10722 series (HAMAMATSU). Recording pipettes were the
478 same as those prepared for TEVC. Currents were sampled at 2 kHz and filtered at 500 Hz.
479 The voltage clamp is maintained at -60 mV and at room temperature. The recording chamber
480 has been designed to perfuse only the part of the oocyte from which the fluorescence emission
481 is simultaneously collected (Figure S3). This chamber has several advantages over chambers
482 that allow to record the current of the entire membrane of the oocytes: 1/ approximately the
483 same population of receptors is recorded in current and fluorescence simultaneously, 2/ the
484 chamber allows for an overexpression of the receptor on the oocyte membrane to increase the
485 fluorescence signal without generating huge currents that make the clamp impossible to
486 maintain during a prolonged period. The oocyte is placed on a hole and the geometry of the
487 perfusion channels has been designed to “suck” the oocyte and stick it to the hole through a
488 Venturi effect, ensuring efficient sealing between the two compartments. A limitation of the
489 chamber is that the design is compatible with only relatively slow perfusion of the agonist, rapid
490 perfusion often expelling the oocyte out of the hole.

491

492 ***Voltage-Clamp Fluorometry data analysis***

493 For each construct, we performed the experiments at least on 2 different batches of oocytes
494 (oocytes from different ovary fragments and different animals) to obtained at least n=5. Data
495 are analyzed by Clampfit software (Molecular Devices) and are filtered by a boxcar filter.
496 Baseline was corrected from leaking currents and measurements were done to the peak of
497 each response. Dose-response curves were fitted to the Hill equation by Prism Graphpad
498 software, and the error bars represent the SEM values. Risetime and decaytime analysis were
499 calculated in Clampfit by monoexponential fits of the onset and the offset of the recordings.
500 Statistical analyses were done using a Student t-test in Prism Graphpad.

501

502 ***Expression in cultured cells***

503 Human Embryonic Kidney 293 (HEK-293) cells were cultured in Dulbecco's modified Eagle's
504 medium (DMEM) with 10% FBS (Invitrogen) in an incubator at 37°C and 5% CO₂. After being
505 PBS washed, trypsin-treated (Trypsine-EDTA; ThermoFisher Scientific) and seeded on petri
506 dishes, cells were transiently transfected using calcium phosphate-DNA co-precipitation with
507 glycine receptor constructs (2 µg DNA) and a construct coding for a green fluorescent protein
508 (0.2 µg). One day after transfection, cells were washed with fresh medium and recordings were
509 carried out within 24 hours.

510

511 ***Outside-out recordings and analysis***

512 Recording currents are obtained with a RK-400 amplifier (BioLogic) using pClamp 10.5
513 software, digitized with a 1550 digidata (Axon instruments). Recording pipettes were obtained
514 from thick-wall borosilicate glass (1.5X0.75mmx7.5cm, Sutter Instrument) using a
515 micropipettes puller (P-1000, Sutter Instrument) and fire-polished with a micro-forge (MF-830,
516 Narishige) to be used at resistances between 7 and 15 M Ω . Micro-pipettes were filled with
517 internal solution (that contain in mM: 152 NaCl, 1 MgCl₂, 10 BAPTA, 10 HEPES; pH adjusted
518 to 7.3 with NaOH solution, osmolarity measured at 335 mOsm). Extracellular solution (in mM:
519 152 NaCl, 1 MgCl₂, 10 HEPES; pH adjusted to 7.3 with NaOH solution and osmolarity was
520 adjusted to 340 mOsm with glucose) was delivered by an automated perfusion system (RSC-
521 200, BioLogic). Agonists' solutions are freshly made before sessions of recordings and are
522 obtained with extracellular solution added with 1 to 100 μ M of glycine (dissolved from stock
523 solution of 1M in water). Acquisition of recordings was performed at the sampling of 20 kHz
524 and low-pass filtered at 1 kHz (using the amplifier 5-pole Bessel filter). Openings are analyzed
525 using Clampfit 10 software and currents were calculated by fitting the all-points histogram
526 distributions of current amplitudes with the sum of two gaussians curves. No further filtering is
527 performed for the analysis.

528

529 ***Molecular Dynamics simulations***

530 Molecular Dynamics simulations of the zebrafish GlyR- α 1 in four different conformational
531 states were carried out: apo-closed (PDB:6PXD), Sy9-closed (PDB:6PXD with Sy9 docked), tau-
532 closed (PDB:6PM3) and tau-open (PDB:6PM2). The zebrafish receptor shares more than 87%
533 of sequence homology with the human receptor according to UNIPROT BLAST alignment. For
534 all the studied systems, the protonation state at pH 7.0 was predicted using the Adaptive
535 Poisson-Boltzmann Solver⁵⁴ (PropKa) via the webserver
536 ("<https://server.poissonboltzmann.org/pdb2pqr>"). Predicted protonation probabilities differed
537 depending on the structure. To homogenize the systems, the most frequent predictions were
538 selected and imposed to all systems: GLU316 was unprotonated, HIS125 protonated in N δ ,
539 HIS217 protonated in N δ and HIS231 protonated in N ϵ . The structures were then embedded
540 in a POPC bilayer and solvated with TIP3P water molecules using CHARMM-GUI Membrane
541 Builder⁵⁵. The CHARMM-36m forcefield⁵⁶ for the protein and CGenFF⁵⁷ for the taurine and
542 strychnine were used for the all-atom molecular dynamics simulations. The simulations were
543 performed using GROMACS 2021.4⁵⁸ with input files generated by CHARMM-GUI Membrane
544 Builder for the minimization and equilibration. In short, 5000 steps of steepest descent were

545 performed, then the system was equilibrated over 6 short simulations in presence of atomic
546 position restrains of decreasing strength, first in NVT, then in NPT ensemble, with the
547 Berendsen thermostat and barostat. The temperature and the pressure were set to 300K and
548 1 bar respectively. Finally, the equilibrated systems were carried on in production for 100 ns
549 at a 2 fs timestep, in the NPT ensemble using V-rescale and Parrinello-Rahman as thermostat
550 and barostat, respectively. In all cases, the LINCS algorithm was used to constrains the H-
551 bonds and the PME served to treat the long-range Coulomb interactions. For each system we
552 produced 5 replicas generated with different initial velocities from the equilibration.
553 MD simulations of the triple-mutant used for the VCF experiments (K159W/Q235C/C57V,
554 following the residue order in the PDB files) were also performed. Initial coordinates of the
555 protein were extracted from the tau-closed (PDB: 6PM3) and tau-open (PDB: 6PM2) cryo-EM
556 structures and the mutations were introduced using the CHARMM-GUI webserver during
557 preparation. The protocol followed to perform the simulations was the same applied to the
558 WT (see above).

559

560 ***Trajectory analysis***

561 The generated trajectories were analyzed using MDanalysis⁵⁹ through Python scripts. Notably
562 we computed the RMSD of the backbone atoms in the ECD, the TMD and the structural core
563 (i.e., the inner and outer beta-sheets in ECD, and the M1-M3 helices in TMD) relative to the
564 initial coordinates from cryo-EM. Additionally, we computed the RMSF decomposed per
565 residue and averaged over the 5 subunits of the receptor. Analyses of the blooming and
566 twisting angles¹⁰ were carried out using WORDOM software
567 (<https://sourceforge.net/p/wordom/codehg/ci/default/tree/>). For these calculations, only a
568 subset of residues was considered, referred to as the core, which is more relevant to monitor
569 the quaternary structure of the receptor. The selected core residues are: 54-69, 73-86, 113-
570 125, 142-154, 165-175, 207-214 for the ECD and residues 225-234, 241-258, 265-288, 297-322
571 for the TMD. Plots were produced using Matplotlib⁶⁰, and the visual representations of the
572 protein with the open-source version of PyMOL⁶¹ (Schrödinger).

573

574 ***Docking***

575 To explore strychnine binding to the various conformational states of the receptor, i.e., apo-
576 closed, tau-closed, and tau-open, we extracted 1 snapshot per nanosecond from the trajectory
577 generated by Molecular Dynamics. By doing so, we ended up with 5 (replica) * 100 (ns) = 500

578 (snapshots) for each system. The molecular docking of strychnine was then executed using
579 QuickVina 2.1⁶² with an exhaustiveness of 8 and a box of dimension 15*15*15Å centered on
580 the previously defined binding sites. For this purpose, we prepared the PDBQT inputs of the
581 receptor using *prepare_receptort4.py* script from MGLTools⁶³. Then, the positions of the 5
582 orthosteric binding sites of a given structure were computed on the fly as the center-of-mass
583 of residues PHE223 of the (+)-subunit and PHE79 of the (-)-subunit using MDAnalysis. Of note,
584 for both tau-open and tau-closed, the receptor was simulated by Molecular Dynamics in the
585 presence of taurine, but the docking of Strychnine was carried out without taurine.

586

587 **Data Availability**

588 Data supporting the findings of this manuscript are available from the corresponding author
589 upon reasonable request. A reporting summary for this Article is available as a Supplementary
590 Information file. Source data are provided with this paper.

591

592 **Competing interest**

593 The authors declare no competing interests

594

595 **Acknowledgements**

596 The work was supported the ERC (Grant no. 788974, Dynacotine), by the 'Agence Nationale
597 de la Recherche' (Grant ANR-18-CE11-0015-01, Pentacontrol), Specific Grant Agreement No.
598 945539 (Human Brain Project SGA3), the doctoral school ED3C and the Foundation pour la
599 Recherche Médicale (to Solène N. Lefebvre). The authors would like to thank Antoine Taly for
600 help in data interpretation, and Alexandre Mourot for critical reading of the manuscript.

601

602 **Authors contribution**

603 SS and SNL set up and performed VCF experiments. LP performed single-channel
604 experiments and some TEVC experiments and VCF experiments. MG designed and
605 constructed the recording chamber. AC and PMR performed MD and docking experiments.
606 SS, SNL, LP, AC, PML, MG, MC and PJC designed the study and analyzed the data. SS, LP,
607 AC, PML, JPC, MC and PJC wrote the manuscript. MC, PJC and JPC acquired funding.

608

609 **References**

- 610 1. Nemezc, Á., Prevost, M. S., Menny, A. & Corringer, P.-J. Emerging Molecular
611 Mechanisms of Signal Transduction in Pentameric Ligand-Gated Ion Channels. *Neuron* **90**,
612 452–470 (2016).
- 613 2. Cecchini, M. & Changeux, J.-P. The nicotinic acetylcholine receptor and its
614 prokaryotic homologues: Structure, conformational transitions & allosteric modulation.
615 *Neuropharmacology* **96**, 137–149 (2015).

- 616 3. Cecchini, M. & Changeux, J.-P. Nicotinic receptors: From protein allostery to
617 computational neuropharmacology. *Molecular Aspects of Medicine* **84**, 101044 (2022).
- 618 4. Indurthi, D. C. & Auerbach, A. Agonist efficiency from concentration-response curves:
619 Structural implications and applications. *Biophysical Journal* **120**, 1800–1813 (2021).
- 620 5. Edelstein, S. J. & Changeux, J.-P. Relationships between Structural Dynamics and
621 Functional Kinetics in Oligomeric Membrane Receptors. *Biophysical Journal* **98**, 2045–2052
622 (2010).
- 623 6. Gupta, S., Chakraborty, S., Vij, R. & Auerbach, A. A mechanism for acetylcholine
624 receptor gating based on structure, coupling, phi, and flip. *Journal of General Physiology*
625 **149**, 85–103 (2017).
- 626 7. Lape, R., Colquhoun, D. & Sivilotti, L. G. On the nature of partial agonism in the
627 nicotinic receptor superfamily. *Nature* **454**, 722–727 (2008).
- 628 8. Lee, W. Y. & Sine, S. M. Principal pathway coupling agonist binding to channel gating
629 in nicotinic receptors. *Nature* **438**, 243–247 (2005).
- 630 9. Rovšnik, U. *et al.* Dynamic closed states of a ligand-gated ion channel captured by
631 cryo-EM and simulations. *Life Sci. Alliance* **4**, e202101011 (2021).
- 632 10. Martin, N. E., Malik, S., Calimet, N., Changeux, J.-P. & Cecchini, M. Un-gating and
633 allosteric modulation of a pentameric ligand-gated ion channel captured by molecular
634 dynamics. *PLoS Comput Biol* **13**, e1005784 (2017).
- 635 11. Calimet, N. *et al.* A gating mechanism of pentameric ligand-gated ion channels. *Proc.*
636 *Natl. Acad. Sci. U.S.A.* **110**, (2013).
- 637 12. Bar-Lev, D. D., Degani-Katzav, N., Perelman, A. & Paas, Y. Molecular Dissection of
638 Cl⁻-selective Cys-loop Receptor Points to Components That Are Dispensable or Essential
639 for Channel Activity. *Journal of Biological Chemistry* **286**, 43830–43841 (2011).
- 640 13. Nury, H. *et al.* One-microsecond molecular dynamics simulation of channel gating in a
641 nicotinic receptor homologue. *Proc. Natl. Acad. Sci. U.S.A.* **107**, 6275–6280 (2010).
- 642 14. Menny, A. *et al.* Identification of a pre-active conformation of a pentameric channel
643 receptor. *eLife* **6**, e23955 (2017).
- 644 15. Lefebvre, S. N., Taly, A., Menny, A., Medjebeur, K. & Corringer, P.-J. Mutational
645 analysis to explore long-range allosteric couplings involved in a pentameric channel receptor
646 pre-activation and activation. *eLife* **10**, e60682 (2021).
- 647 16. Basak, S. *et al.* High-resolution structures of multiple 5-HT₃AR-setron complexes
648 reveal a novel mechanism of competitive inhibition. *eLife* **9**, e57870 (2020).
- 649 17. Polovinkin, L. *et al.* Conformational transitions of the serotonin 5-HT₃ receptor.
650 *Nature* **563**, 275–279 (2018).
- 651 18. Masiulis, S. *et al.* GABA_A receptor signalling mechanisms revealed by structural
652 pharmacology. *Nature* **565**, 454–459 (2019).
- 653 19. Yu, J. *et al.* Mechanism of gating and partial agonist action in the glycine receptor.
654 *Cell* **184**, 957-968.e21 (2021).
- 655 20. Rahman, Md. M. *et al.* Structural mechanism of muscle nicotinic receptor
656 desensitization and block by curare. *Nat Struct Mol Biol* **29**, 386–394 (2022).
- 657 21. Lape, R., Plested, A. J. R., Moroni, M., Colquhoun, D. & Sivilotti, L. G. The 1K276E
658 Startle Disease Mutation Reveals Multiple Intermediate States in the Gating of Glycine
659 Receptors. *Journal of Neuroscience* **32**, 1336–1352 (2012).
- 660 22. Bormann, J., Hamill, O. P. & Sakmann, B. Mechanism of anion permeation through
661 channels gated by glycine and gamma-aminobutyric acid in mouse cultured spinal neurones.
662 *The Journal of Physiology* **385**, 243–286 (1987).
- 663 23. Du, J., Lü, W., Wu, S., Cheng, Y. & Gouaux, E. Glycine receptor mechanism

664 elucidated by electron cryo-microscopy. *Nature* **526**, 224–229 (2015).

665 24. Talwar, S. & Lynch, J. W. Investigating ion channel conformational changes using
666 voltage clamp fluorometry. *Neuropharmacology* **98**, 3–12 (2015).

667 25. Bode, A. *et al.* New Hyperekplexia Mutations Provide Insight into Glycine Receptor
668 Assembly, Trafficking, and Activation Mechanisms. *Journal of Biological Chemistry* **288**,
669 33745–33759 (2013).

670 26. Han, L., Talwar, S., Wang, Q., Shan, Q. & Lynch, J. W. Phosphorylation of $\alpha 3$ Glycine
671 Receptors Induces a Conformational Change in the Glycine-Binding Site. *ACS Chem.*
672 *Neurosci.* **4**, 1361–1370 (2013).

673 27. Shan, Q., Han, L. & Lynch, J. W. β Subunit M2–M3 Loop Conformational Changes
674 Are Uncoupled from $\alpha 1$ β Glycine Receptor Channel Gating: Implications for Human
675 Hereditary Hyperekplexia. *PLoS ONE* **6**, e28105 (2011).

676 28. Wang, Q. & Lynch, J. W. Activation and Desensitization Induce Distinct
677 Conformational Changes at the Extracellular-Transmembrane Domain Interface of the
678 Glycine Receptor. *Journal of Biological Chemistry* **286**, 38814–38824 (2011).

679 29. Pless, S. A. & Lynch, J. W. Ligand-specific Conformational Changes in the $\alpha 1$ Glycine
680 Receptor Ligand-binding Domain. *Journal of Biological Chemistry* **284**, 15847–15856 (2009).

681 30. Pless, S. A. & Lynch, J. W. Magnitude of a Conformational Change in the Glycine
682 Receptor $\beta 1$ - $\beta 2$ Loop Is Correlated with Agonist Efficacy. *Journal of Biological Chemistry*
683 **284**, 27370–27376 (2009).

684 31. Pless, S. A., Dibas, M. I., Lester, H. A. & Lynch, J. W. Conformational Variability of
685 the Glycine Receptor M2 Domain in Response to Activation by Different Agonists. *J. Biol.*
686 *Chem.* **282**, 36057–36067 (2007).

687 32. Kumar, A. *et al.* Mechanisms of activation and desensitization of full-length glycine
688 receptor in lipid nanodiscs. *Nat Commun* **11**, 3752 (2020).

689 33. Cerdan, A. H., Martin, N. É. & Cecchini, M. An Ion-Permeable State of the Glycine
690 Receptor Captured by Molecular Dynamics. *Structure* **26**, 1555-1562.e4 (2018).

691 34. Mansoor, S. E., DeWitt, M. A. & Farrens, D. L. Distance Mapping in Proteins Using
692 Fluorescence Spectroscopy: The Tryptophan-Induced Quenching (TrIQ) Method.
693 *Biochemistry* **49**, 9722–9731 (2010).

694 35. Doose, S., Neuweiler, H. & Sauer, M. A Close Look at Fluorescence Quenching of
695 Organic Dyes by Tryptophan. *ChemPhysChem* **6**, 2277–2285 (2005).

696 36. Wilkins, M. E., Caley, A., Gielen, M. C., Harvey, R. J. & Smart, T. G. Murine startle
697 mutant *Nmf11* affects the structural stability of the glycine receptor and increases
698 deactivation: Glycine receptor $\alpha 1N46K$ and startle syndrome. *J Physiol* **594**, 3589–3607
699 (2016).

700 37. Langosch, D., Herbold, A., Schmieden, V., Borman, J. & Kirsch, J. Importance of Arg-
701 219 for correct biogenesis of alpha 1 homooligomeric glycine receptors. *FEBS Lett.* **336**,
702 540–544 (1993).

703 38. Bode, A. & Lynch, J. W. Analysis of Hyperekplexia Mutations Identifies
704 Transmembrane Domain Rearrangements That Mediate Glycine Receptor Activation. *J. Biol.*
705 *Chem.* **288**, 33760–33771 (2013).

706 39. O’Shea, S. M. Propofol Restores the Function of ‘Hyperekplexic’ Mutant Glycine
707 Receptors in *Xenopus* Oocytes and Mice. *Journal of Neuroscience* **24**, 2322–2327 (2004).

708 40. Laube, B., Langosch, D., Betz, H. & Schmieden, V. Hyperekplexia mutations of the
709 glycine receptor unmask the inhibitory subsite for β -amino-acids: *NeuroReport* **6**, 897–900
710 (1995).

711 41. Schmieden, V., Kuhse, J. & Betz, H. Agonist pharmacology of neonatal and adult

712 glycine receptor alpha subunits: identification of amino acid residues involved in taurine
713 activation. *EMBO J* **11**, 2025–2032 (1992).

714 42. Jan, D. D. S., David - Watine, B., Korn, H. & Bregestovski, P. Activation of human $\alpha 1$
715 and $\alpha 2$ homomeric glycine receptors by taurine and GABA. *The Journal of Physiology* **535**,
716 741–755 (2001).

717 43. Schmieden, V. & Betz, H. Pharmacology of the inhibitory glycine receptor: agonist
718 and antagonist actions of amino acids and piperidine carboxylic acid compounds. *Mol*
719 *Pharmacol* **48**, 919–927 (1995).

720 44. Kim, J. J. & Hibbs, R. E. Direct Structural Insights into GABAA Receptor
721 Pharmacology. *Trends in Biochemical Sciences* **46**, 502–517 (2021).

722 45. Cerdan, A. H. *et al.* The Glycine Receptor Allosteric Ligands Library (GRALL).
723 *Bioinformatics* **36**, 3379–3384 (2020).

724 46. Fourati, Z. *et al.* Structural Basis for a Bimodal Allosteric Mechanism of General
725 Anesthetic Modulation in Pentameric Ligand-Gated Ion Channels. *Cell Reports* **23**, 993–1004
726 (2018).

727 47. Nury, H. *et al.* X-ray structures of general anaesthetics bound to a pentameric ligand-
728 gated ion channel. *Nature* **469**, 428–431 (2011).

729 48. Sauguet, L. *et al.* Crystal structures of a pentameric ligand-gated ion channel provide
730 a mechanism for activation. *Proc. Natl. Acad. Sci. U.S.A.* **111**, 966–971 (2014).

731 49. Lape, R., Colquhoun, D. & Sivilotti, L. G. On the nature of partial agonism in the
732 nicotinic receptor superfamily. *Nature* **454**, 722–727 (2008).

733 50. Laha, K. T., Ghosh, B. & Czajkowski, C. Macroscopic Kinetics of Pentameric Ligand
734 Gated Ion Channels: Comparisons between Two Prokaryotic Channels and One Eukaryotic
735 Channel. *PLoS ONE* **8**, e80322 (2013).

736 51. Dahan, D. S. *et al.* A fluorophore attached to nicotinic acetylcholine receptor M2
737 detects productive binding of agonist to the site. *Proceedings of the National Academy of*
738 *Sciences* **101**, 10195–10200 (2004).

739 52. Mouro, A., Bamberg, E. & Rettinger, J. Agonist- and competitive antagonist-induced
740 movement of loop 5 on the α subunit of the neuronal $\alpha 4\beta 4$ nicotinic acetylcholine receptor. *J*
741 *Neurochem* **105**, 413–424 (2008).

742 53. Gielen, M., Barilone, N. & Corringer, P.-J. The desensitization pathway of GABAA
743 receptors, one subunit at a time. *Nat Commun* **11**, 5369 (2020).

744 54. Jurrus, E. *et al.* Improvements to the APBS biomolecular solvation software suite.
745 *Protein Science* **27**, 112–128 (2018).

746 55. Wu, E. L. *et al.* CHARMM-GUI *Membrane Builder* toward realistic biological
747 membrane simulations. *J. Comput. Chem.* **35**, 1997–2004 (2014).

748 56. Huang, J. *et al.* CHARMM36m: an improved force field for folded and intrinsically
749 disordered proteins. *Nat Methods* **14**, 71–73 (2017).

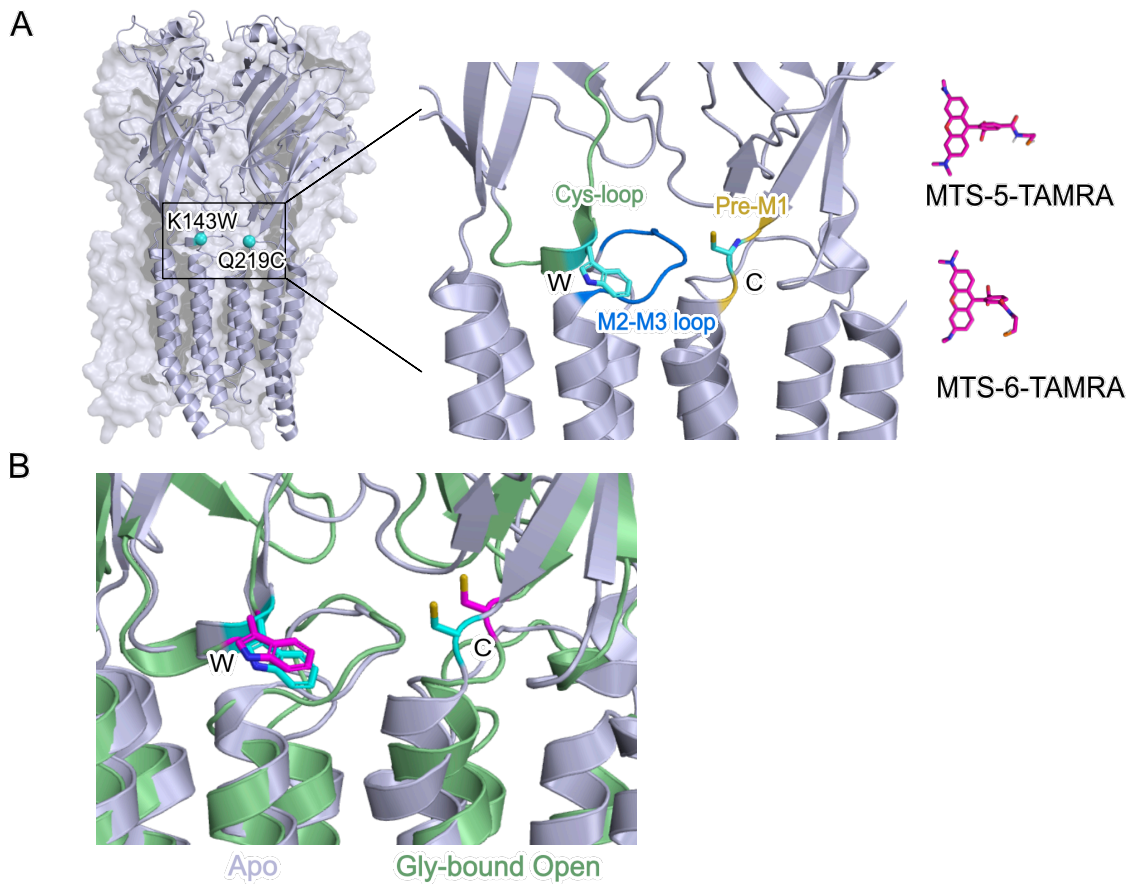
750 57. Vanommeslaeghe, K., Raman, E. P. & MacKerell, A. D. Automation of the CHARMM
751 General Force Field (CGenFF) II: Assignment of Bonded Parameters and Partial Atomic
752 Charges. *J. Chem. Inf. Model.* **52**, 3155–3168 (2012).

753 58. Abraham, M. J. *et al.* GROMACS: High performance molecular simulations through
754 multi-level parallelism from laptops to supercomputers. *SoftwareX* **1–2**, 19–25 (2015).

755 59. Michaud-Agrawal, N., Denning, E. J., Woolf, T. B. & Beckstein, O. MDAAnalysis: A
756 toolkit for the analysis of molecular dynamics simulations. *J. Comput. Chem.* **32**, 2319–2327
757 (2011).

758 60. Hunter, J. D. Matplotlib: A 2D Graphics Environment. *Comput. Sci. Eng.* **9**, 90–95
759 (2007).

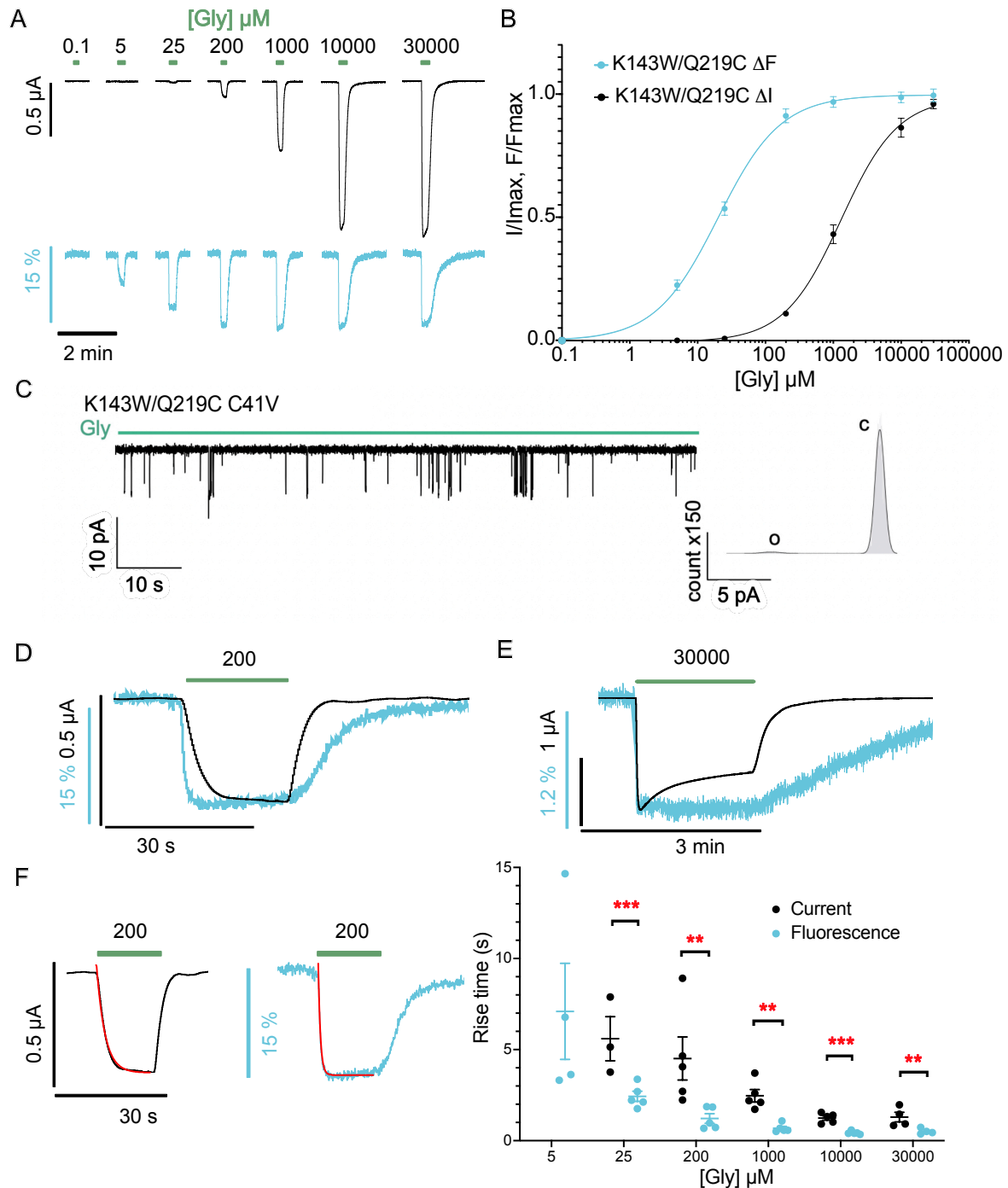
- 760 61. Schrödinger, L. L. C., The PyMOL Molecular Graphics System, Version 2.5, (2015).
761 62. Alhossary, A., Handoko, S. D., Mu, Y. & Kwoh, C.-K. Fast, accurate, and
762 reliable molecular docking with QuickVina 2. *Bioinformatics* **31**, 2214–2216 (2015).
763 63. Morris, G. M. *et al.* AutoDock4 and AutoDockTools4: Automated docking with
764 selective receptor flexibility. *J. Comput. Chem.* **30**, 2785–2791 (2009).



766

767 **Figure 1. Localization of K143W/Q219C sensor in the $\alpha 1$ glycine receptor structure.**

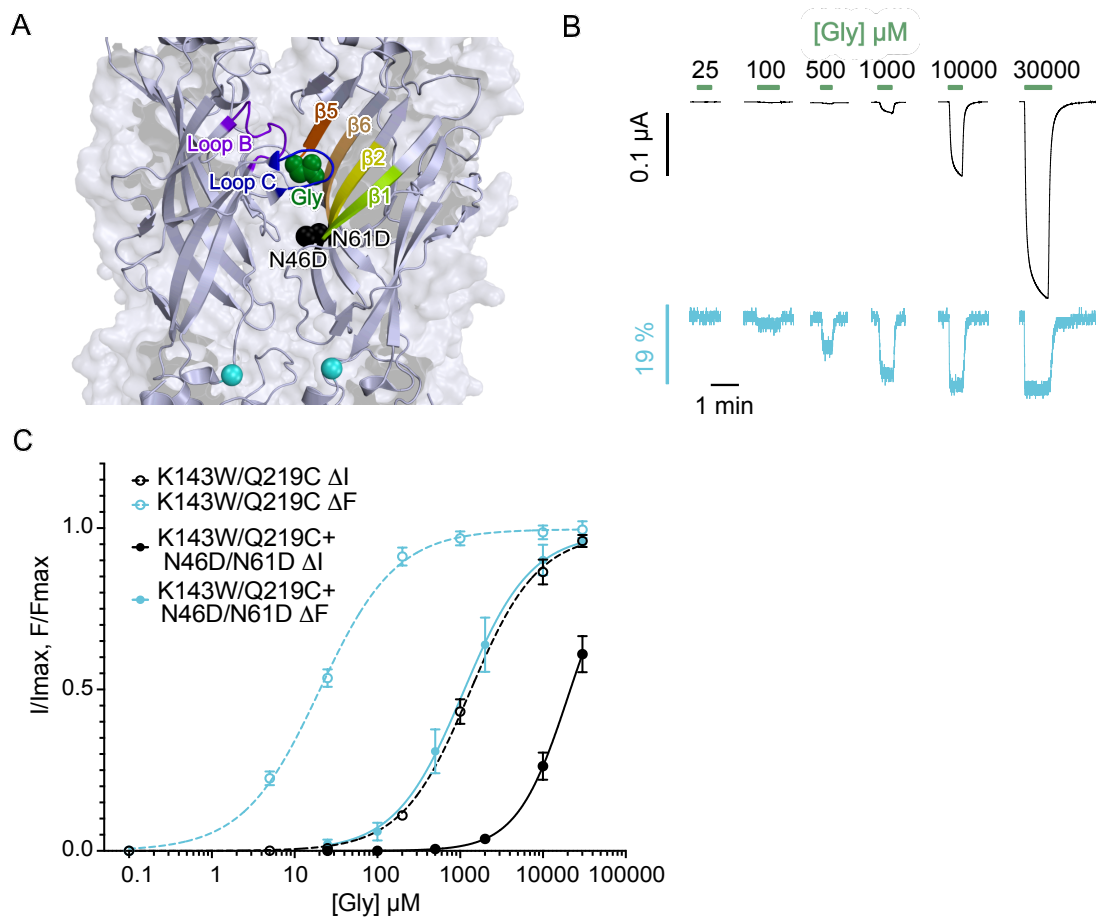
768 (A) Side view of the zebrafish $\alpha 1$ glycine receptor structure in Apo state (PDB:6PXD) showing the position of the mutated residues
 769 K143W in Cys-loop and Q219C in Pre-M1 loop. Right panel: representation of the two isomers of 5(6)-
 770 carboxytetramethylrhodamine methanethiosulfonate (MTS-TAMRA) used for the labeling of the mutated cysteine. (B) Structural
 771 comparison of the quenching sensor K143W/Q219C between the Apo state in grey (PDB:6PXD) and Gly-bound open state in
 772 green (PDB:6PM6), residues are presented in cyan for apo state and magenta for Gly-bound open state. The distance calculated
 773 between the C α of the two residues varied from 12,9 Å for Apo state to 15,6 Å for Open state.



774
775
776
777
778
779
780
781
782
783
784
785
786
787
788
789
790

Figure 2. Electrophysiological and fluorescence characterization of K143W/Q219C sensor by VCF on C41V GlyR.

(A) Representative VCF recordings on oocytes of the mutant labeled with MTS-TAMRA (black for current and cyan for fluorescence). Glycine application triggers a current variation and a fluorescence quenching phenomenon with a maximum of fluorescence variation that reach $12.1 \pm 1.1\%$ of $\Delta F/F$. At low concentration of glycine (under $25 \mu\text{M}$), only fluorescence quenching is observed without any current. (B) ΔI (black) and ΔF (cyan) dose-response curves with mean \pm S.E.M. values ($n=5$). (C) Left panel: representative trace of single-channel recordings obtained in outside-out configuration recorded at -100mV with concentrations of glycine at $100\mu\text{M}$. Right panel: histograms of current amplitude representing the closed state (c) and the open state (o). (D) Superimposition of the current and fluorescence recordings evoked by $200 \mu\text{M}$ glycine application showing that the onset of the fluorescence is faster than the onset of current and that the fluorescence offset is slower than the current offset. (E) Representative recording with a high glycine concentration (30mM) application showing that the desensitization triggered by a prolonged glycine application does not impact the fluorescence variation. A mean decrease of $30.63 \pm 4.90\%$ of the current elicited by 30 mM of glycine is observed ($n=4$). (F) Left panel: examples of single exponential fitting (red line) of the current (left) and fluorescence (right) traces onset. Right panel: time constants τ (onset) values obtained via single exponential fitting with mean and S.E.M. error bars at different glycine concentrations. Unpaired student t-test indicates the significance of the difference between fluorescence and current onset (**: $P < 0,005$; ***: $P < 0,0005$).



791
792
793
794
795
796
797
798

Figure 3. Effect of N46D/N61D mutations on ΔI and ΔF curves of K143W/Q219C on C41V GlyR.

(A) Side view of zebrafish $\alpha 1$ glycine receptor structure in Apo state (PDB:6PXD) with details of loops and β -sheets forming the orthosteric site and the localization of N46D/N61D mutations. Glycine molecule is represented in green and N46D/N61D mutated residues (spheres) in black. (B) Representative VCF recordings of the mutant K143W/Q219C + N46D/N61D (current in black and fluorescence in cyan). (C) ΔI (cyan) and ΔF (black) dose-response curves with mean \pm S.E.M. show a parallel shift of the current and fluorescence curves of the K143W/Q219C/N46D/N61D mutant (solid line; n=5) compared to K143W/Q219C alone (dotted line).

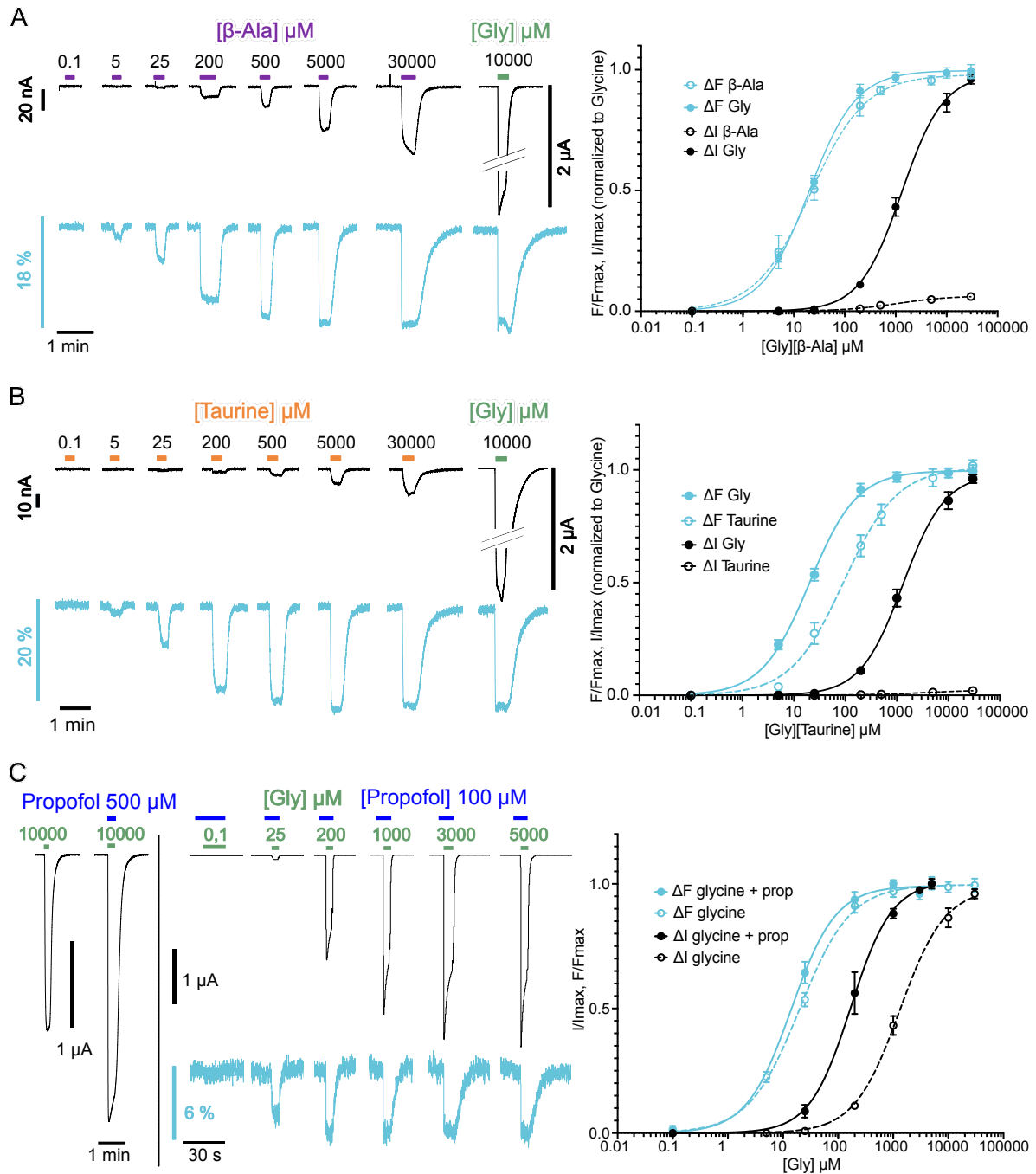
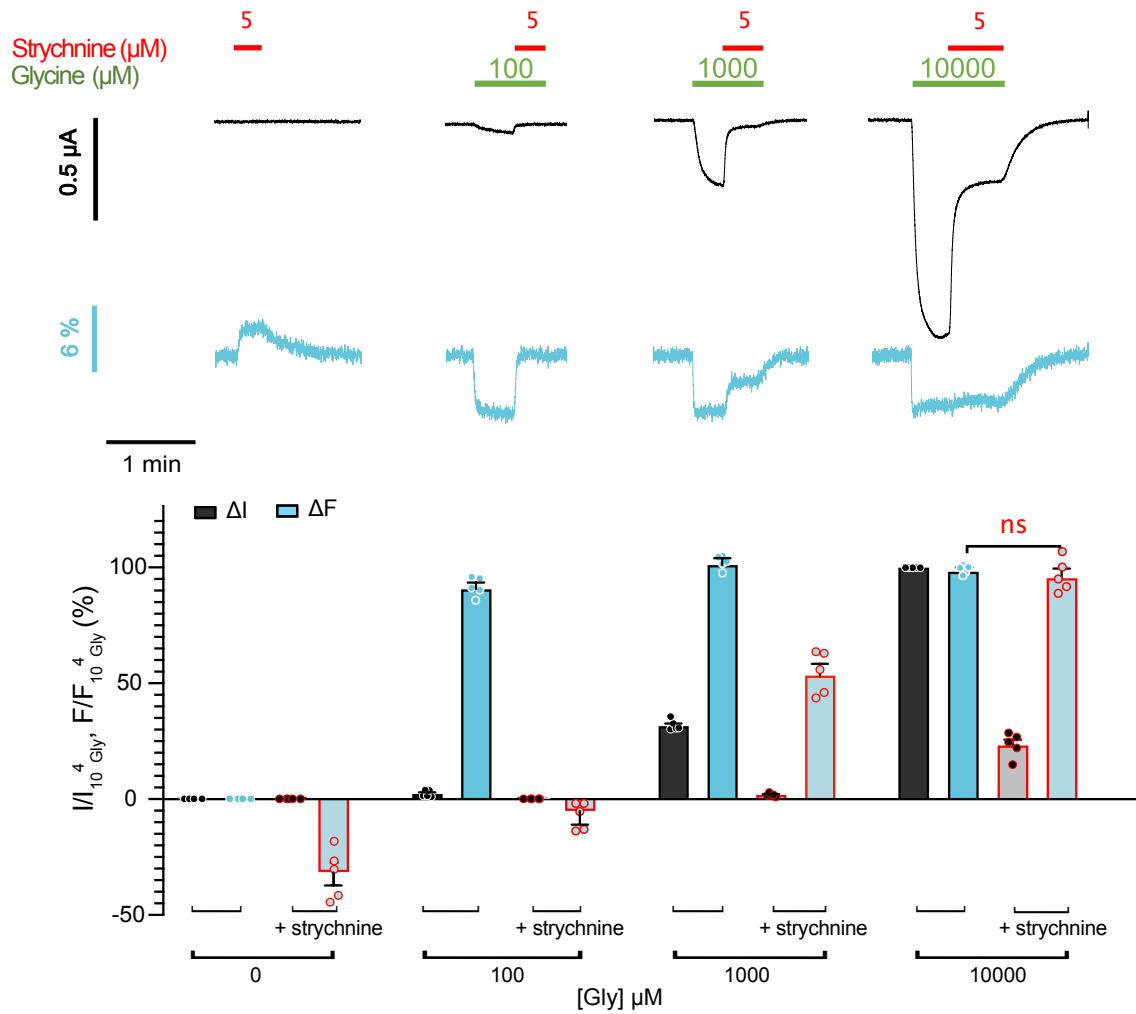


Figure 4. Electrophysiological and fluorescence characterization of partial agonist (β -alanine and taurine) and propofol effects on K143W/Q219C sensor on C41V GlyR.

(A) Right panel: Representative VCF recordings on an oocyte challenged with both β -alanine and glycine. Left panel: representative VCF recording on oocytes under β -alanine application. Right panels: the ΔI (cyan) and ΔF (black) curves (normalized to the glycine maximal response recorded on each individual oocyte) with mean and S.E.M. for K143W/Q219C under glycine (solid line) and β -alanine (dotted line) application. The ΔF curves for both molecules are superimposed but the efficacy of β -alanine to activate the receptor is lower than that of glycine ($6.1 \pm 2.2\%$ of glycine maximum response in current, $n=6$). (B) Right panel: Representative VCF recordings on an oocyte challenged with both taurine and glycine. Left panel: representative VCF recording in oocytes under taurine application. Right panel: ΔI (cyan) and ΔF (black) curves (normalized to the glycine maximal response recorded on each individual oocyte) with mean and S.E.M. for K143W/Q219C under glycine (solid line) and taurine (dotted line) application. Taurine elicits only $2.0 \pm 1.4\%$ of glycine maximum current, $n=6$. (C) Left panels: Representative VCF recording on an oocyte challenged with maximal glycine concentration in presence and absence of propofol at 500 μM . Middle panel: representative VCF recording on an oocyte under glycine and propofol co-application. Right panel: ΔI (cyan) and ΔF (black) dose response curves with mean and S.E.M. for K143W/Q219C under glycine and propofol (solid line, $n=6$) and glycine alone (dotted line) application.

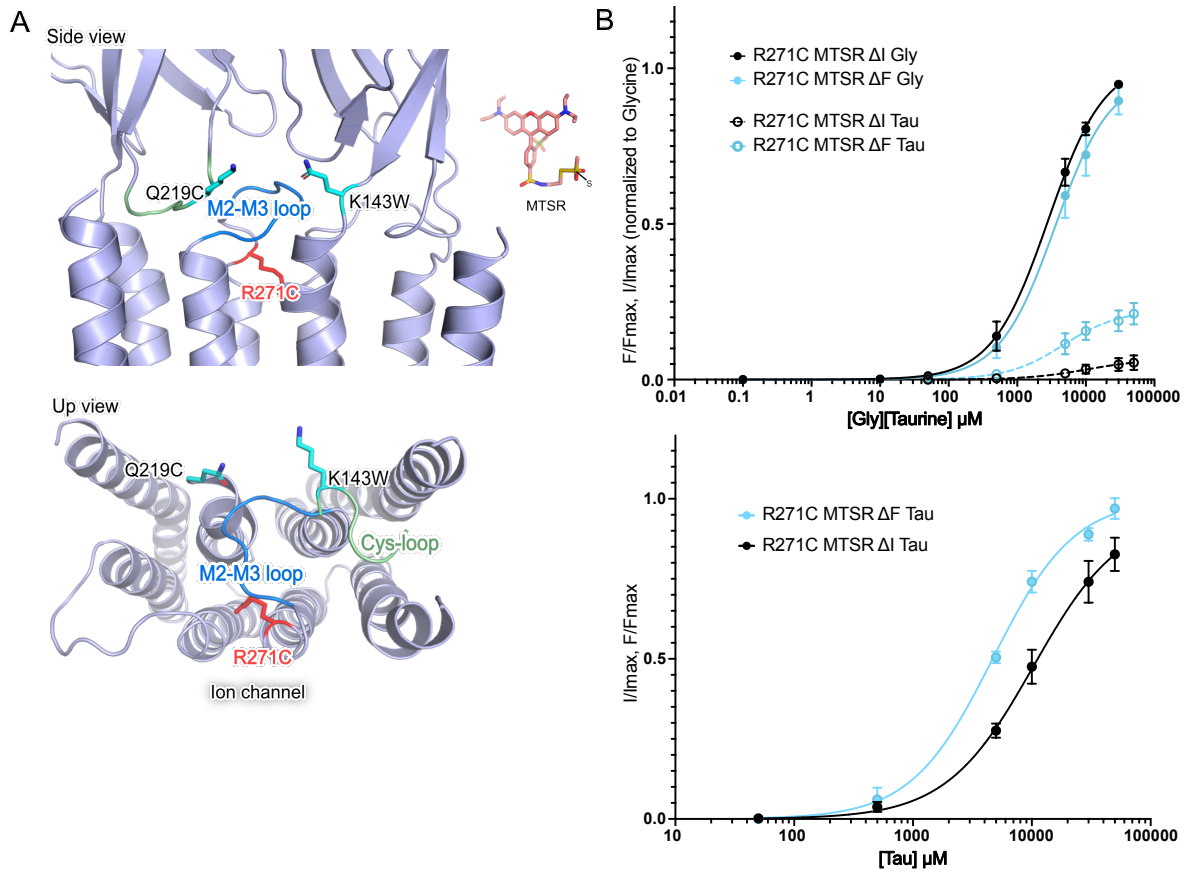
799
800
801
802
803
804
805
806
807
808
809
810
811
812
813
814
815



816
817
818
819
820
821
822
823
824
825

Figure 5. Differential inhibition of strychnine on fluorescence and current on K143W/Q219C sensor on C41V GlyR.

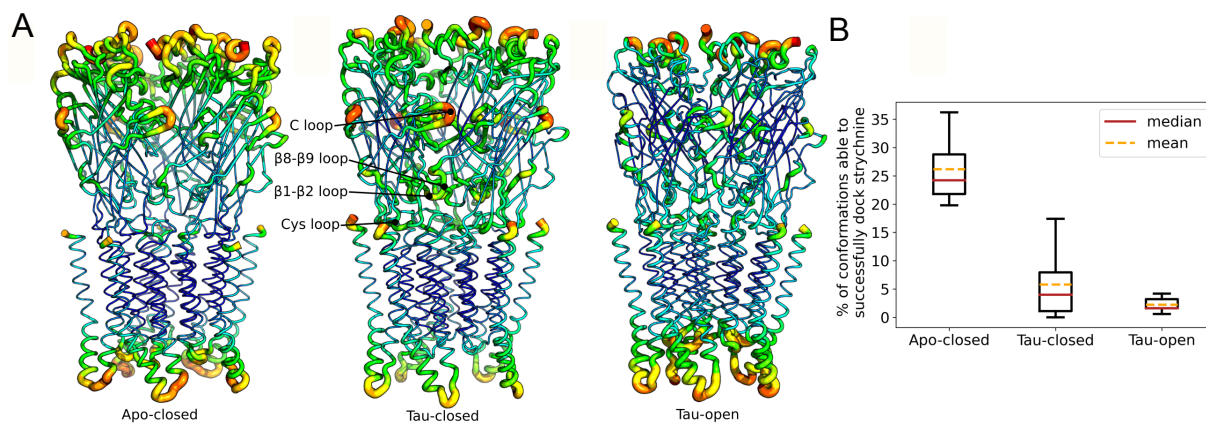
Upper left panel: Representative VCF recording where application of strychnine alone at 5 μM triggers a fluorescence dequenching. Upper right panels: glycine is applied at different concentrations first alone (green bar) and then in mixture with 5 μM strychnine (red bar plus green bar), showing differential strychnine-elicited inhibition of current and fluorescence depending on the glycine concentration (n=5). Lower panel: fluorescence (cyan) and current (black) variations normalized to the fluorescence and current variations under 10mM of glycine (mean and S.E.M. (n=5)). "ns" Denotes not significantly different between the ΔF (under glycine) and ΔF (under strychnine inhibition); $P < 0.05$ (Unpaired student t-test).



826
827
828
829
830
831
832
833

Figure 6. Characterization of R271C by VCF on C41V GlyR.

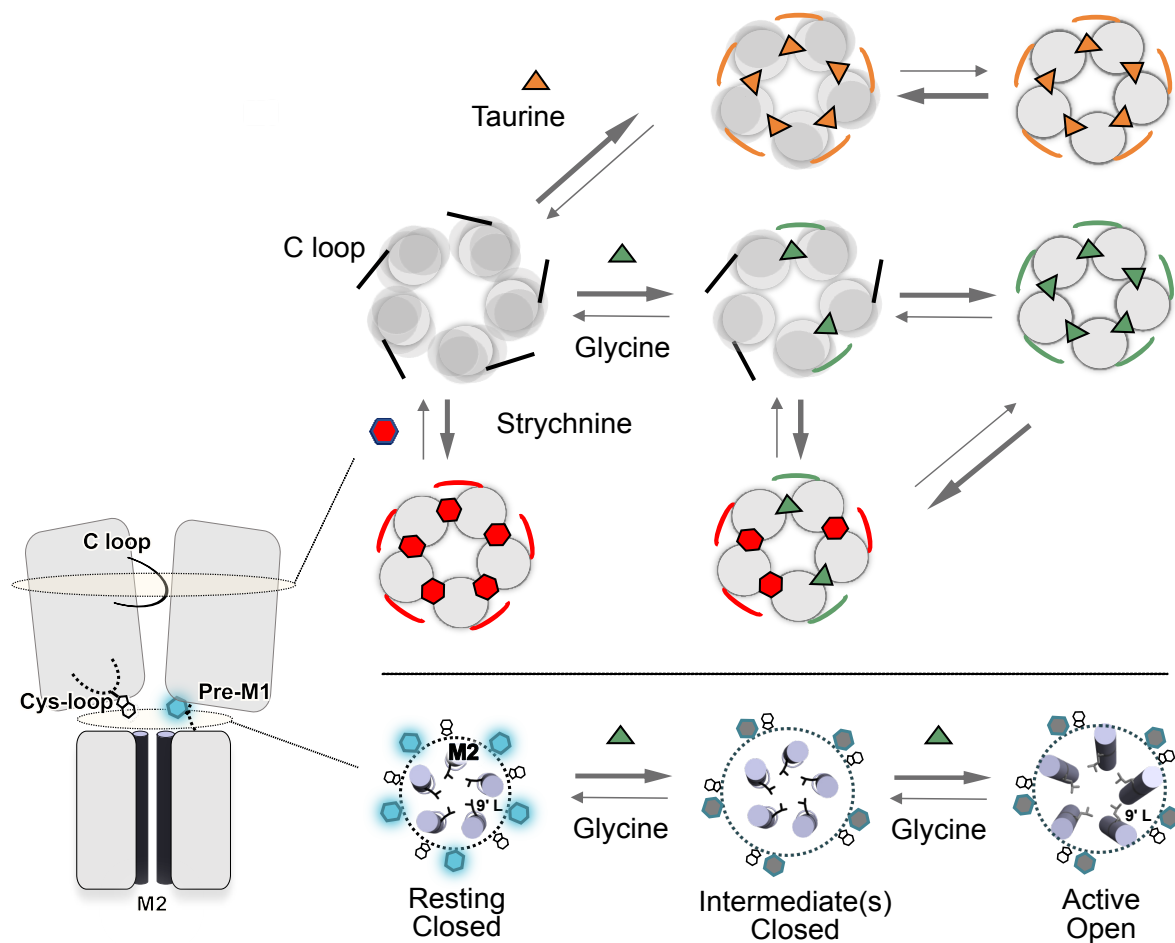
(A) Localization of the R271C mutation on the GlyR compared to the sensor K143W/Q219C (PDB:6PXD). (B) Upper panel: ΔI (cyan) and ΔF (black) dose response curves (normalized to the glycine maximal response recorded on each individual oocyte) with mean and S.E.M. for R271C under glycine (solid line) and taurine (dotted line) application. Taurine elicits only $5.4 \pm 2.3\%$ of glycine maximum current, $n=5$. Lower panel: ΔI (cyan) and ΔF (black) dose response curves normalized to maximum value with mean and S.E.M. for R271C under taurine application.



834
 835
 836
 837
 838
 839
 840
 841
 842
 843

Figure 7. Dynamic “personality” of the tau-closed state.

(A). Root-mean-square fluctuations (RMSF) from the average structure extracted from 0.5 μ s MD simulations in explicit solvent/membrane are shown for three conformational states of GlyR captured by cryo-EM. Apo-closed corresponds to the resting state, tau-open to the active state of the receptor. For each state, RMSF values ranging from 0.5 Å to 4.5 Å are shown by the color (from blue to red) and the thickness (from thin to thick) of the sausage representation (B). State-based docking of strychnine. Relative strychnine-binding affinities for apo-closed, tau-closed, and tau-open was probed by docking strychnine to an ensemble of 500 protein snapshots sampled by MD and comparing the success rate of docking; i.e. a docking experiment was considered as successful if the docking score was within 10% of the score obtained in the strychnine-bound X-ray structure (stry-closed). The mean (yellow) or median (red) dashed lines show that strychnine binding in tau-closed is significantly stronger than in tau-open.



844
845
846
847
848
849
850
851

Figure 8. Hypothetical transition pathway of the GlyR.

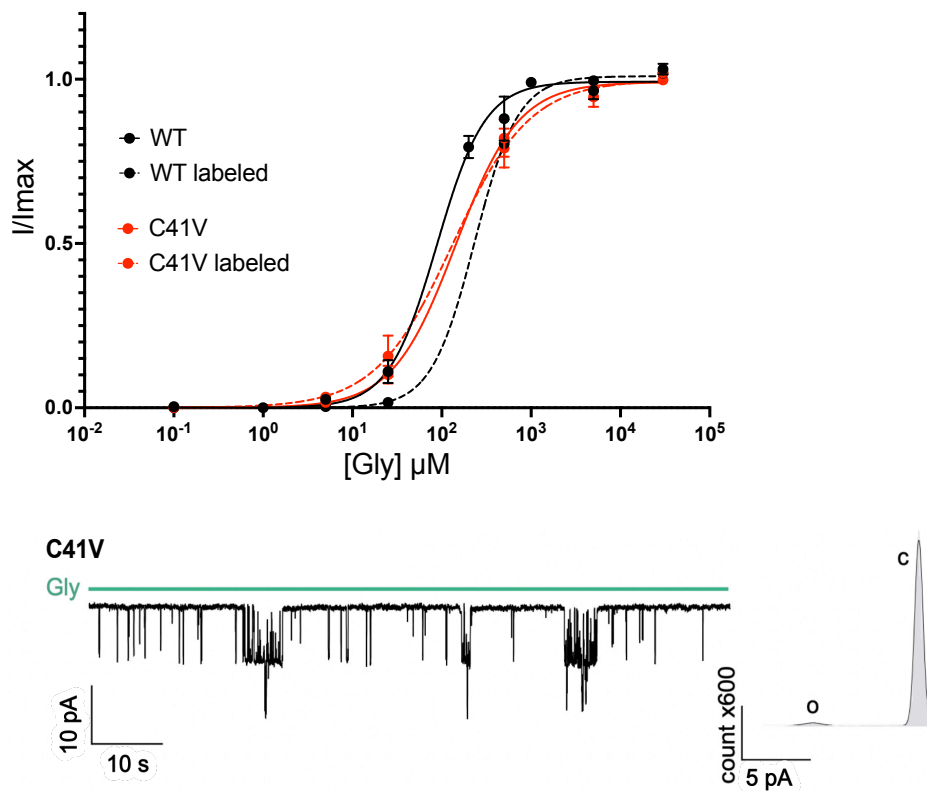
Left panel: side-view cartoon representation of two subunits of the GlyR. C loop contributing to the orthosteric site, the quenching sensor, the TAMRA (hexagon) and tryptophane (indole) are represented. Upper panel: top view representation of the receptor in different conformations with the ECD of each subunit shown in circle and C loop as a line. Lower panel: top view representation of the TMD showing the M2 helices and the L9' that closes the pore in the resting and intermediate(s) conformations. The black circle represents positions where the fluorescent quenching sensor is grafted. The indole goes closer to the TAMRA from the resting to the intermediate(s) conformations, generating a quenching of fluorescence.

852 **Table 1. EC₅₀ values for current and fluorescence responses to glycine at labeled and unlabeled C41V-**
 853 **GlyRα1 mutants.**

	EC ₅₀ ^{current} (μM)	n _H	EC ₅₀ ^{fluo} (μM)	n _H	n
WT without C41V MTS-TAMRA	165.84 ± 14.06	1.55 ± 0.08			5
WT without C41V unlabeled	79.30 ± 11.34	2.16 ± 0.36			8
WT MTS-TAMRA	162.87 ± 43.21	1.18 ± 0.13			5
WT unlabeled	152.40 ± 28.87	1.33 ± 0.26			4
Q219C MTS-TAMRA	56.80 ± 6.65	1.84 ± 0.13	550.95 ± 67.55	1.71 ± 0.15	6
Q219C unlabeled	70.52 ± 3.47	2.23 ± 0.46			5
K143W/Q219C MTS-TAMRA	1541.12 ± 338.71	1.06 ± 0.11	21.00 ± 2.26	0.96 ± 0.10	5
K143W/Q219C unlabeled	2485.20 ± 145.08	1.04 ± 0.03			5
K143W/Q219C/N46D/N61D MTS-TAMRA	23029.40 ± 4281.72	1.41 ± 0.04	1428.52 ± 396.81	1.12 ± 0.06	5
K143W/Q219C V280M MTS-TAMRA	22.79 ± 11.24	0.544 ± 0.06			5
K143W/Q219C R271Q MTS-TAMRA			118.09 ± 15.11	0.81 ± 0.06	6
R271C MTSR	2863.40 ± 766.67	1.36 ± 0.11	4517.60 ± 1335.87	1.12 ± 0.11	5

854
855

Supplementary Figures



857

858

859

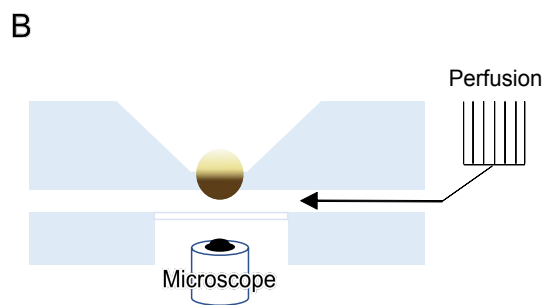
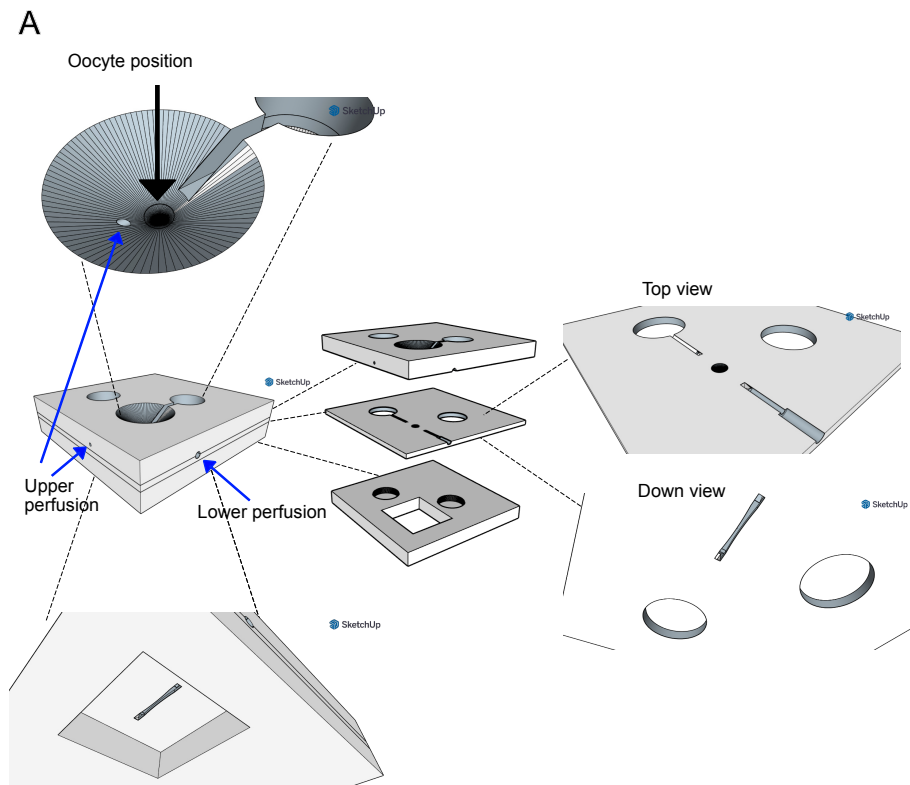
Supplementary Figure 1. Control experiments showing labeled and unlabeled WT and C41V background mutant.

860

Upper panel: current dose-response curves with mean \pm the S.E.M. of the WT (black) and C41V (red) mutant without labeling in solid line and with MTS-TAMRA labeling in dotted line ($n=4$). The labeling of the WT triggers a weak loss of function of the receptor, while the C41V mutant is not impacted by the labeling. Lower left panel: single channel recording obtained by outside-out patch-clamp on HEK293 cells of the C41V mutant evoked by glycine application. The C41V mutant displays wild-type like glycine-elicited dose-response curve (TEVC) and unitary conductance as studied by outside-out single channel recording (Bormann *et al.*, 1987 and 1993). Lower right panel: histograms of current amplitude representing the closed state (c) and the open state (o).

866

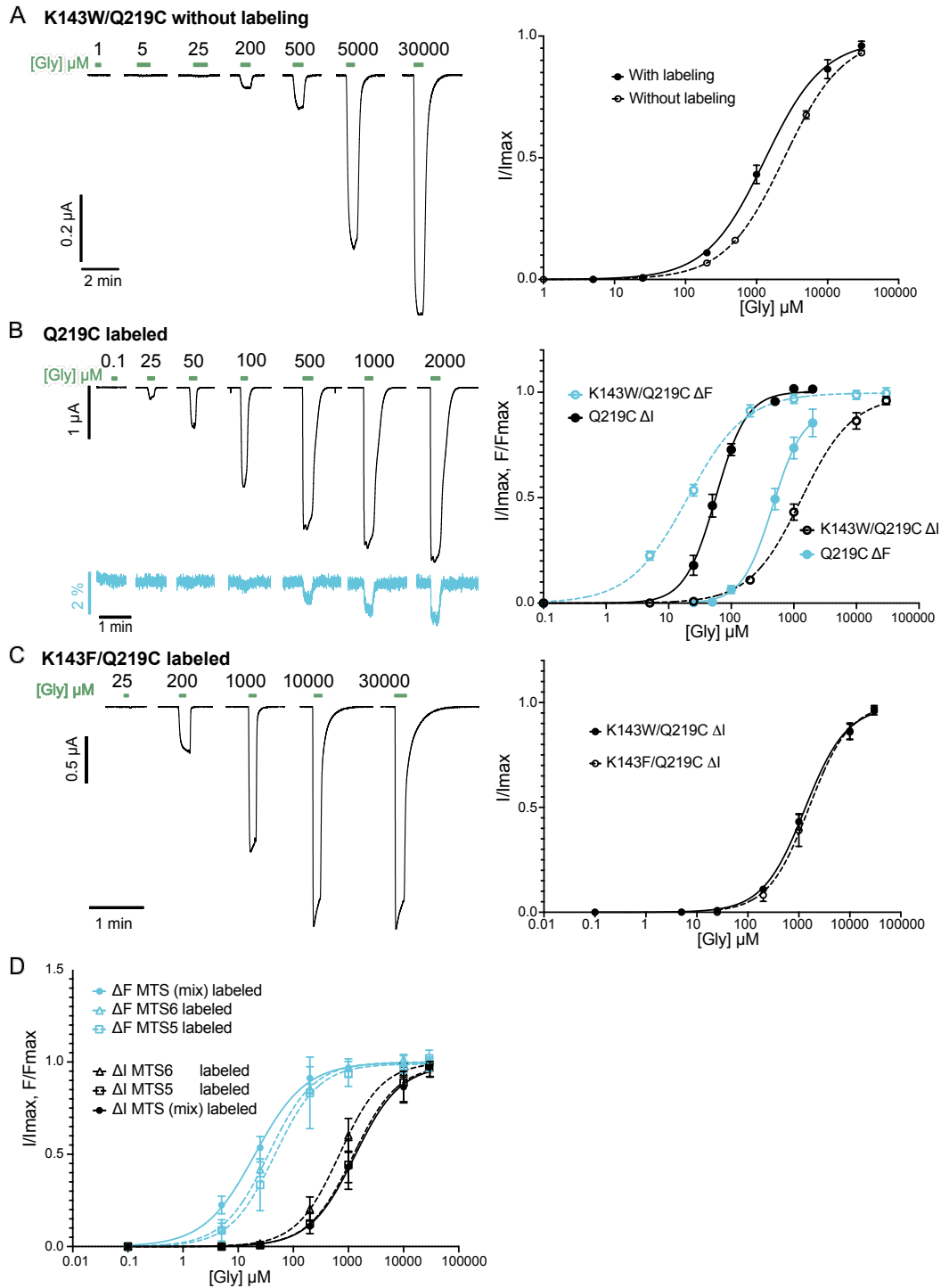
867



868
869
870
871
872
873

Supplementary Figure 2. Blueprint of the perfusion recording chamber and schematic view of the voltage-clamp fluorometry set-up used in this study.

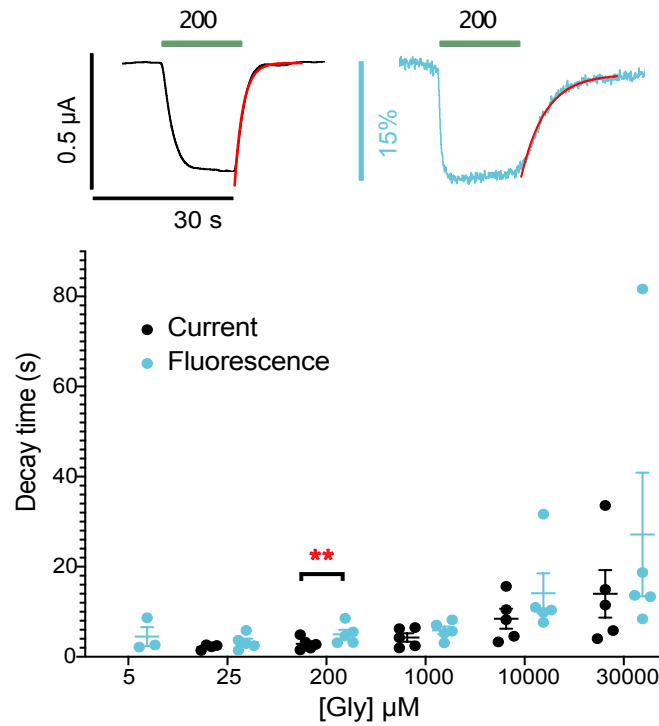
(A) The recording chamber has been designed to perfuse only the portion of the animal pole that is imaged by fluorescence. A venturi effect allows to seal the oocyte in the chamber without any activation of receptors expressed on the upper side of the oocyte. (B) Schematic view of the voltage-clamp fluorometry set-up used in this study.



874
875
876
877
878
879
880
881
882
883
884
885
886
887
888

Supplementary Figure 3. Control experiments showing labeled Q219C, unlabeled K143W/Q219C, labeled K143F/Q219C and MTS-5/6-TAMRA VCF data on C41V GlyR.

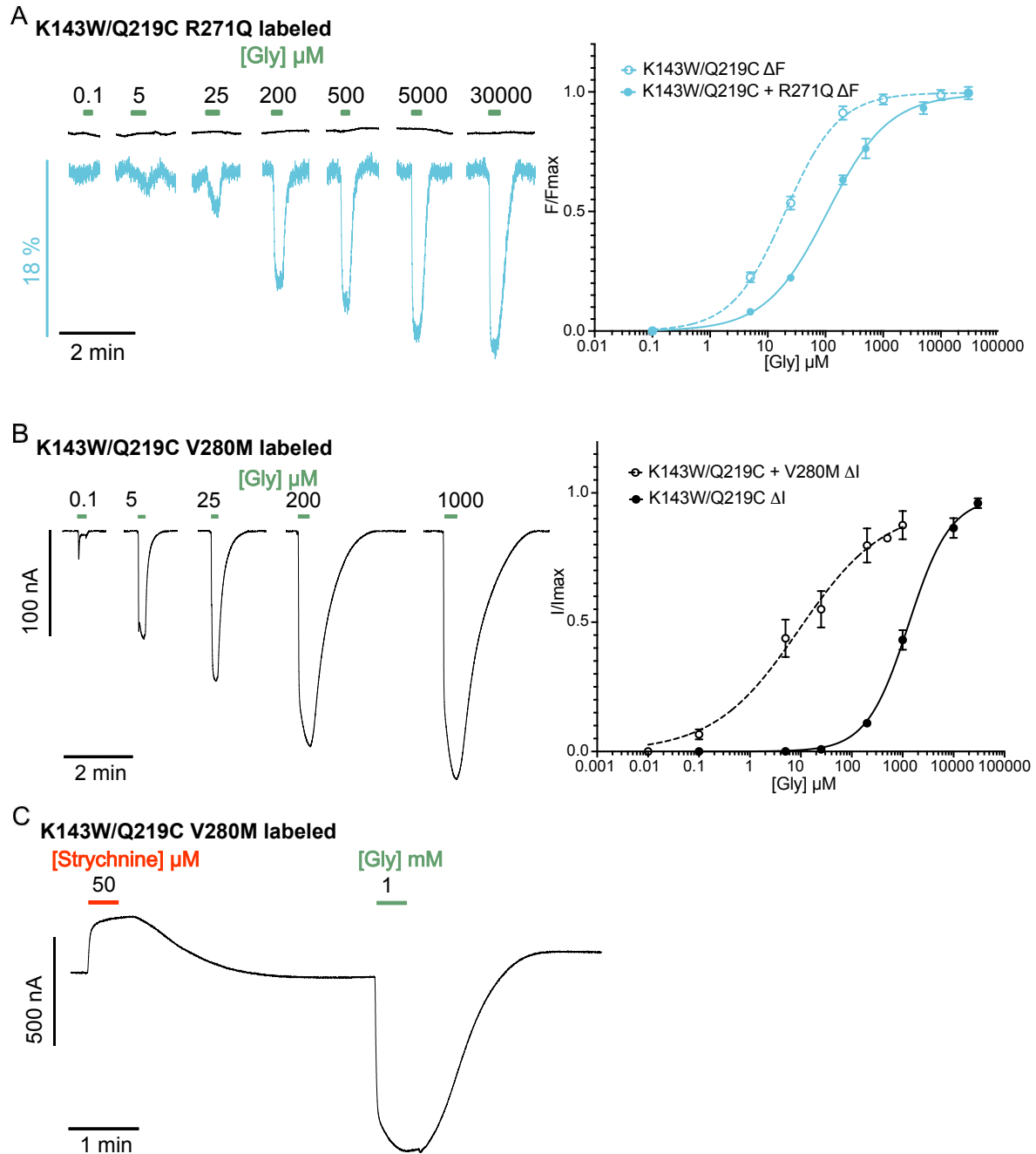
(A) Left panel: representative current recording of K143W/Q219C without labeling. Right panel: dose-response curves with mean \pm the S.E.M. of K143W/Q219C labeled with MTS-TAMRA (solid line) and unlabeled (dotted line, $n=5$). The labeling of the receptors triggers a small gain-of-function. (B) Left panel: representative VCF recordings of Q219C labeled with MTS-TAMRA. Fluorescence variation reaches 1.97 ± 0.49 % of $\Delta F/F_{\text{max}}$ ($n=6$). Right panel: VCF glycine dose-response curves with mean \pm the S.E.M. of Q219C labeled with MTS-TAMRA (solid line, $n=6$) compared to the K143W/Q219C (dotted line). For Q219C, the fluorescence (cyan) is shifted to a higher concentration of glycine compared to the current variation (black), with an EC_{50}^{fluo} that is 10-fold higher than the EC_{50}^{current} . (C) Left panel: representative current recording of K143F/Q219C labeled with MTS-TAMRA. Right panel: VCF glycine dose-response curves with mean \pm the S.E.M. of K143W/Q219C labeled with MTS-TAMRA (solid line, $n=5$) compared to the K143F/Q219C (dotted line, $n=5$). No fluorescence variation is elicited by glycine for the mutant K143F/Q219C. (D) Fluorescence (cyan) and current (black) dose-response curves with mean \pm the S.E.M. of mutant K143W/Q219C labeled with isomers of MTS-TAMRA (solid line, round point), MTS-6-TAMRA (dotted line, triangular point, $n=5$) and MTS-5-TAMRA (dotted line, rectangular point, $n=5$).



889
890
891
892
893
894

Supplementary Figure 4. Single exponential fitting of the current and fluorescence traces offset of K143W/Q219C sensor on C41V GlyR.

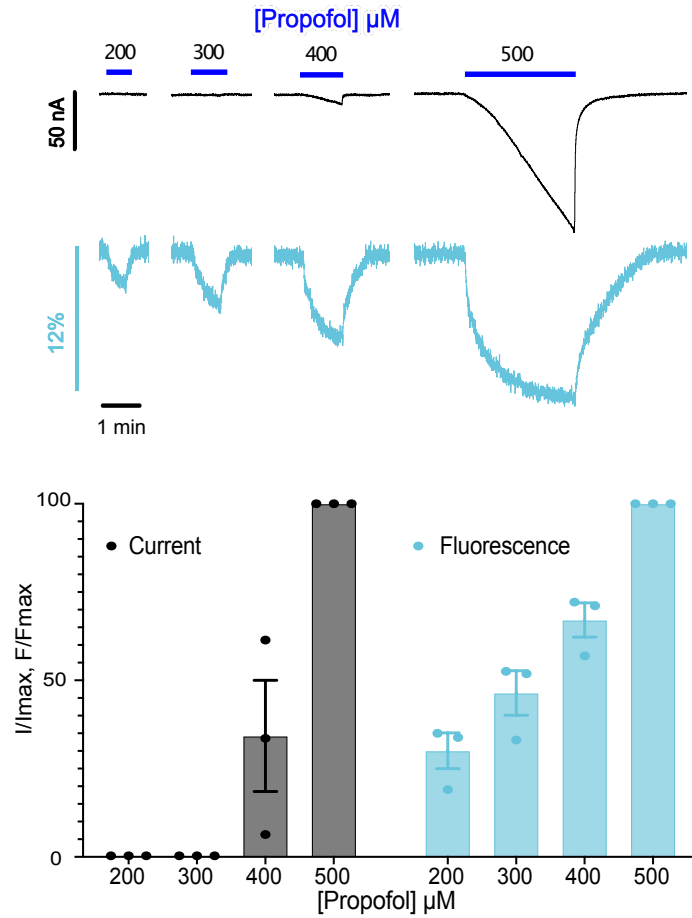
Upper panel: single exponential fitting (red line) of the current and fluorescence traces offset. Lower panel: time constants τ (offset) values obtained via single exponential fitting with mean and S.E.M. error bars at different glycine concentrations. Unpaired student t-test indicates the significance of the difference between fluorescence and current offset (**: $P < 0,005$; ***: $P < 0,0005$).



895
896
897
898
899
900
901
902
903
904
905

Supplementary Figure 5. VCF experiments of hyperekplexia mutations on C41V GlyR.

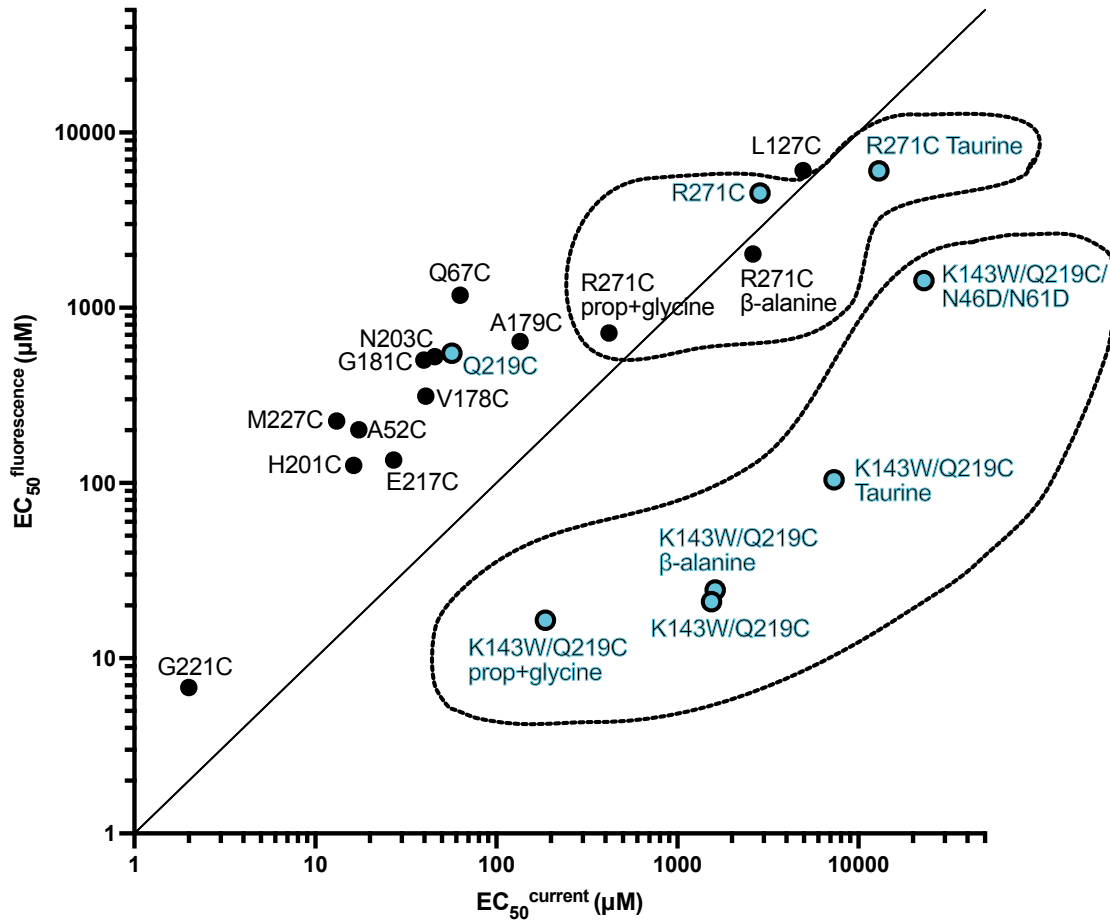
(A) Left panel: representative VCF recordings of K143W/Q219C/R271Q labeled with MTS-TAMRA (no currents observed in this construct). Fluorescence variation reaches 1.97 ± 0.49 % of $\Delta\text{F}/\text{Fmax}$ ($n=6$). Right panel: VCF glycine dose-response curves with mean \pm the S.E.M. of K143W/Q219C/R271Q labeled with MTS-TAMRA (solid line, $n=6$) compared to the K143W/Q219C (dotted line). (B) Left panel: representative VCF recording of K143W/Q219C/V280M labeled with MTS-TAMRA. Note that no change in fluorescence is observed in this construct. Right panel: dose-response curves with mean \pm the S.E.M. of K143W/Q219C (solid line) and K143W/Q219C/V280M labeled with MTS-TAMRA (dotted line, $n=5$). (C) Representative VCF recording of K143W/Q219C/V280M under strychnine (red) application compared to glycine (green) application. The currents inhibited by strychnine produce a 31.14 ± 6.72 % inhibition current compared to the maximum current elicited by 1mM glycine.



906
907
908
909
910
911
912
913
914

Supplementary Figure 6. Electrophysiological and fluorescence characterization of K143W/Q219C sensor on C41V GlyR with propofol.

Upper panel: representative VCF recording under different concentration (200 to 500 μM) of propofol application. Lower panel: fluorescence (cyan) and current (black) variations normalized to the fluorescence and current variations under 500 μM of propofol (mean and S.E.M. (n=3)). At low concentrations of propofol (less than 300 μM), a fluorescence variation is observed without any current. Of note, the slow kinetics of the fluorescence and current traces is likely due to the slow kinetics of partition of propofol into the plasma membrane (Heusser *et al.*, 2018).



915

916

917 **Supplementary Figure 7 : plot representing the $EC_{50}^{\text{fluorescence}}$ as a function of the EC_{50}^{current} of labeled**
 918 **cysteine mutants from VCF data**

919 Labeled mutants that are colored black are taken from previously published articles (Pless et al J. Biol. Chem 282, 36057–36067

920 (2007), JBC 284, 15847–15856 (2009), JBC 284, 27370–27376 (2009), and those colored cyan are from this work. The data

921 points correspond to activation by glycine, unless when other ligands are specified. Mutants showing $EC_{50}^{\text{fluorescence}}/EC_{50}^{\text{current}}$ values

922 lower than 1, which are indicative of an intermediate phenotype, are located below the diagonal. The plot shows that the vast

923 majority of the Pless mutants do not display an intermediate phenotype, with the exception of R271C activated by the partial

924 agonists beta-alanine and taurine. The plot shows that most mutants displaying a $EC_{50}^{\text{fluorescence}}/EC_{50}^{\text{current}}$ higher than 1 display an

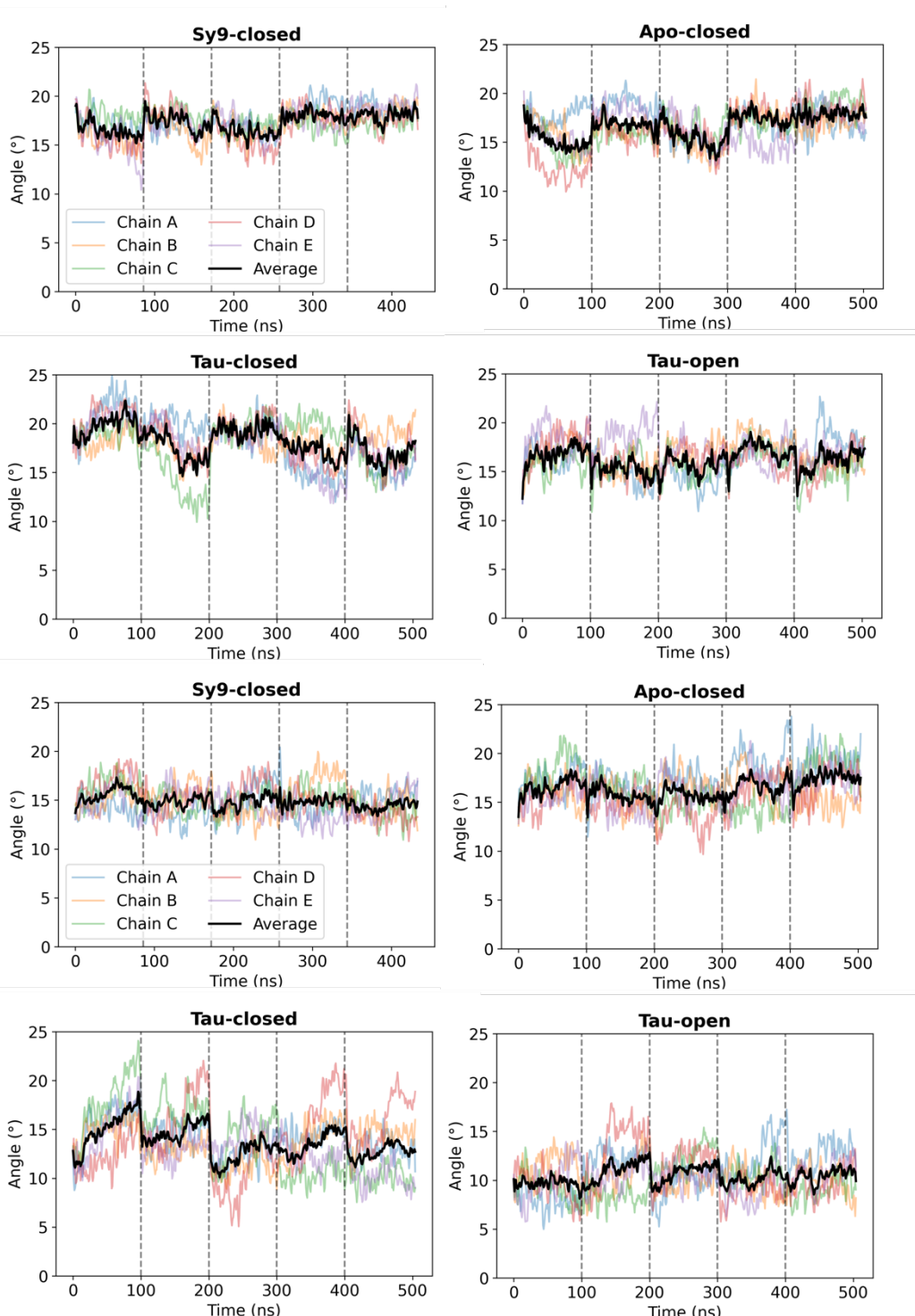
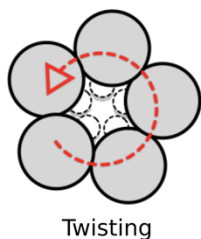
925 EC_{50}^{current} in the WT-range, while those displaying a $EC_{50}^{\text{fluorescence}}/EC_{50}^{\text{current}}$ lower than 1 (indicative of an intermediate phenotype),

926 are characterized by a marked loss of function, with the exception of the condition in glycine plus propofol (on K143W/Q219C).

927

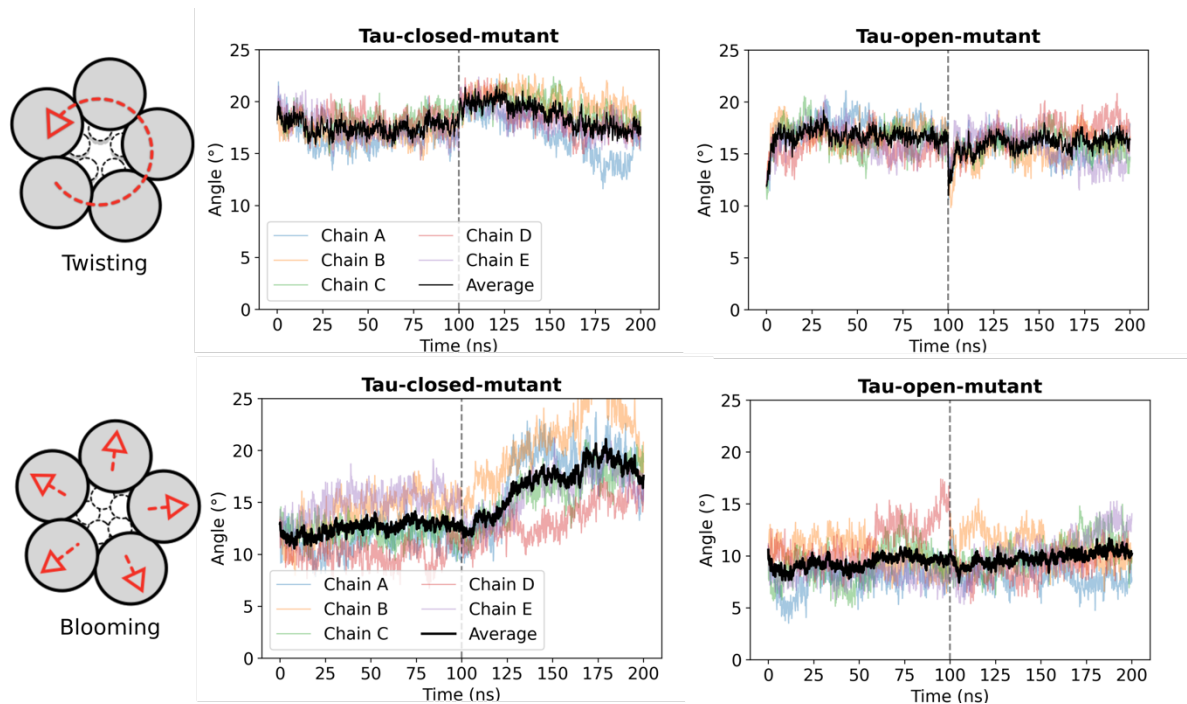
928

929



930
931
932
933
934
935
936
937
938
939
940
941
942

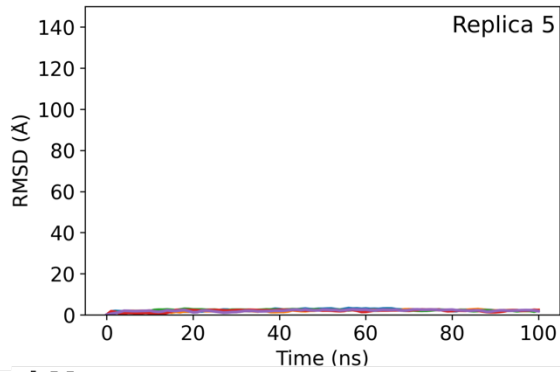
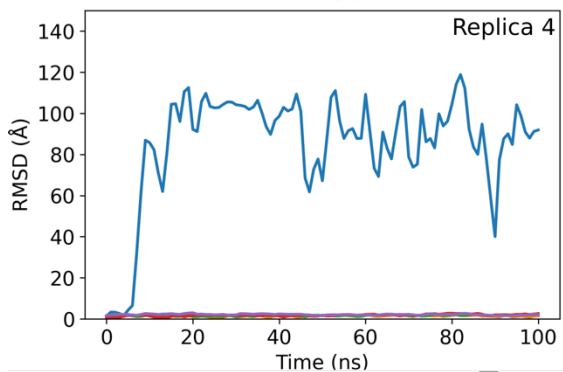
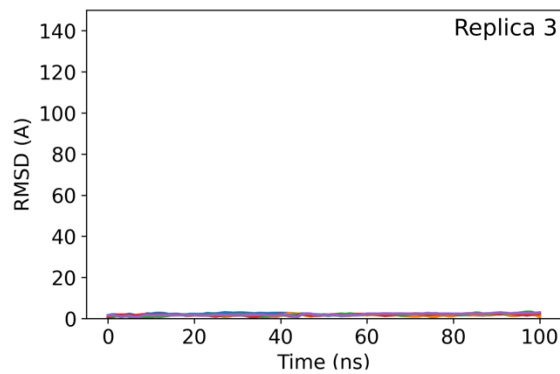
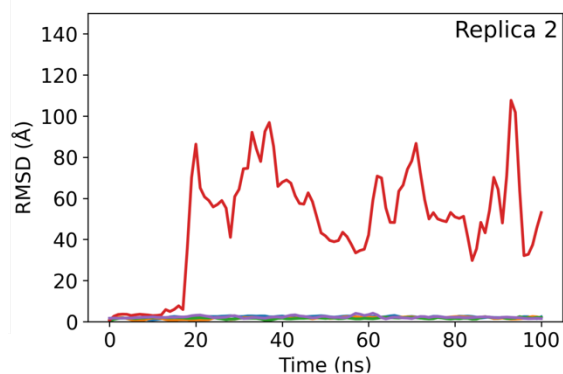
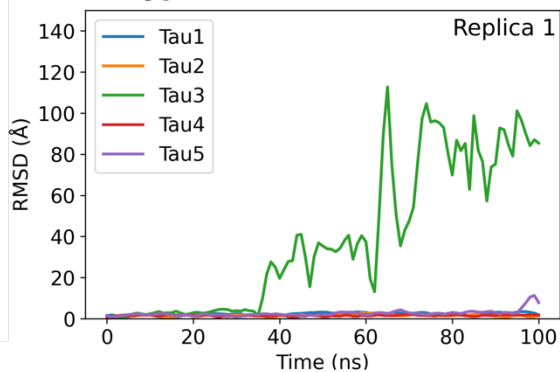
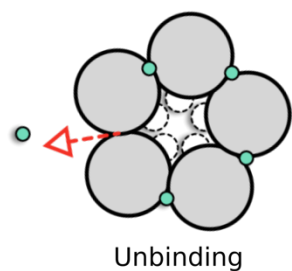
Supplementary Figure 8. Twisting and blooming angles in MD simulations of the wild type (WT). The time series of the twisting angle (upper panel) and the blooming angle (lower panel) are shown for each set of simulations (i.e., apo-closed, sy9-closed, tau-closed and tau-open). Each set includes five independent replicas whose time series are separated by dashed vertical lines. Color-coded lines correspond to individual subunits, the thick black line shows the average over the pentamer. Concerning receptor twisting (upper panel), no clear trend is observed. The average twisting angle fluctuates from 16° to 23° in the closed-channel conformations and is slightly lower in tau-open. The blooming angle (lower panel) is more informative. Its average value is stable around 10° in tau-open, while it increases to 16° in sy9-closed and apo-closed. In tau-closed, receptor blooming is more pronounced in replicas 1 and 2 due to the spontaneous unbinding of taurine (two unbinding events in replica 1, and one in replica 2), whereas it remains close to 13° in the other replicas. Overall, this analysis suggests that receptor's un-blooming, i.e., the compaction of the ECD, is associated with agonist binding, as seen in the apo-closed versus tau-closed and tau-open simulations. Additionally, an increase of the blooming angle in tau-closed is observed because of taurine unbinding. Finally, the active state represented by tau-open features a stable un-bloomed conformation.



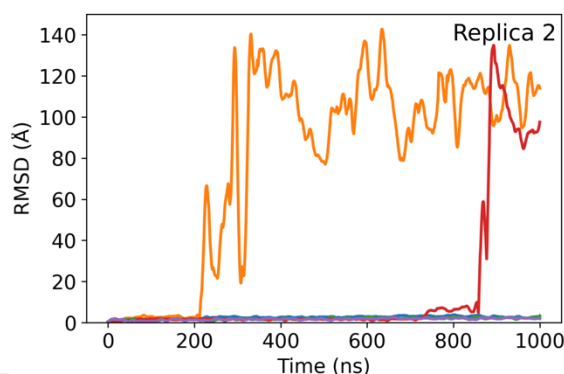
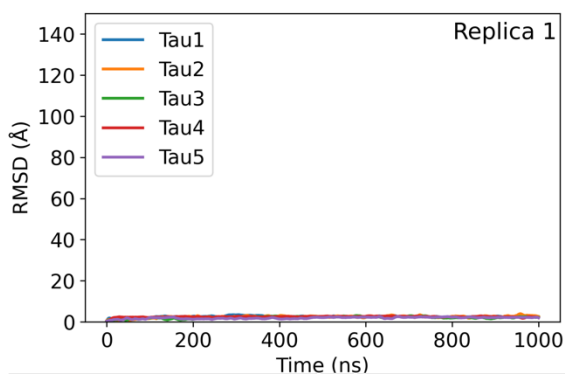
943
 944 **Supplementary Figure 9. Twisting and blooming angles in MD simulations of the triple mutant (K143W/Q219C/C41V).**
 945 The time series of twisting angle (upper panel) and the blooming angle (lower panel) are show for each set of simulations (tau-
 946 closed and tau-open). Each set includes two independent replicas whose time series are separated by dashed vertical lines.
 947 Color-coded lines correspond to individual subunits, the thick black line shows the average over the pentamer. The behaviour of
 948 the triple-mutant simulations is WT-like. The twisting angle does not show any trend, being slightly higher in the tau-close
 949 simulations (around 17.5°) than in tau-open (around 16.3°). Regarding the blooming angle, the difference between two sets of
 950 simulations is more pronounced. The average for tau-closed is 15.2° while for tau-open it fluctuates around 9.7°. As for WT,
 951 spontaneous taurine unbinding was observed in replica 2 (Fig.S9). The impact of taurine unbinding is shown by the blooming
 952 angle, which increases through time in replica 2, while it stays stable in replica 1. Overall, the simulation results for the mutant are
 953 like those collected for WT. Therefore, the WT simulations presented in this manuscript are appropriate to explore the
 954 conformational dynamics of the mutant used in the VCF experiments.
 955

956
 957
 958

Tau-closed Wild-Type



Tau-closed Mutant



959
960
961
962
963
964
965
966

Supplementary Figure 10. Spontaneous unbinding of taurine in MD simulations of the tau-closed state. The RMSD of taurine was monitored over time without optimal superimposition of the atomic coordinates to account for both translational and rotational motions of the ligand. If the RMSD is small and stable, taurine remains bound. When the RMSD increases suddenly, taurine unbinds. Results for the WT simulations are shown on top, those for the K143W/Q219C/C41V triple mutant on bottom. In the WT simulations, two taurine ligands unbind in replica 1, one in replica 2, and one in replica 4. In the mutant simulations, two taurine unbind in replica 2 and none in replica 1.

967 **Supplementary Table 1. EC₅₀ values for current and fluorescence responses to β-alanine and taurine at**
 968 **labeled K143W/Q219C and R271C mutants on C41V GlyR.**
 969

K143W/Q219C	EC ₅₀ ^{current} (μM)	n _H	EC ₅₀ ^{fluo} (μM)	n _H	n
Taurine	7325.35 ± 2442.41	0.78 ± 0.11	104.46 ± 18.28	0.88 ± 0.05	6
β-alanine	1615.78 ± 502.42	1.22 ± 0.39	24.51 ± 5.96	0.83 ± 0.10	6
Propofol + glycine	186.59 ± 40.49	1.38 ± 0.13	16.49 ± 6.82	1.73 ± 0.78	6
R271C	EC ₅₀ ^{current} (μM)	n _H	EC ₅₀ ^{fluo} (μM)	n _H	n
Taurine	12972.00 ± 2364.96	1.24 ± 0.24	6044.00 ± 1054.84	1.36 ± 0.32	5

970 **Supplementary Table 2. ΔFmax/F (%) and ΔFmax/ΔImax (%) values to glycine for C41V GlyRα1 mutants.**
 971
 972
 973
 974
 975

	ΔFmax/F (%)	ΔFmax/ΔImax (%)
Q219C	1.97 ± 0.21	0.21 ± 0.03
Q219C/K143W	12.2 ± 1.03	1.27 ± 0.43
Q219C/K143W/N46D/N61D	15.19 ± 5.14	4.15 ± 0.76

976 **Supplementary Table 3. τ_{rise} and τ_{decay} values for fluorescence and current at labeled K143W/Q219C on**
 977 **C41V GlyR.**
 978
 979
 980
 981

Risetime		
Concentration (μM)	τ current (s)	τ fluorescence (s)
5		7.10 ± 2.64
25	4.95 ± 0.43	2.43 ± 0.29
200	4.51 ± 1.18	1.22 ± 0.27
1000	2.46 ± 0.34	0.68 ± 0.10
10000	1.24 ± 0.12	0.43 ± 0.04
30000	1.29 ± 0.26	0.51 ± 0.08
Decaytime		
Concentration (μM)	τ current (s)	τ fluorescence (s)
5		4.00 ± 1.56
25	2.20 ± 0.28	3.28 ± 0.83
200	2.88 ± 0.59	5.00 ± 1.11
1000	4.28 ± 0.94	5.86 ± 0.96
10000	8.45 ± 2.21	14.11 ± 4.95
30000	13.98 ± 5.28	27.15 ± 15.34

982
 983
 984

985
986
987

Supplementary Table 4. α -RMSD, blooming angle and twisting angle average values for the WT and triple-mutant MD simulations. Only the last 80 ns of simulation were considered.

System	RMSD (\AA)	Blooming angle ($^\circ$)	Twist angle ($^\circ$)
Tau_open WT	1.62 +/- 0.02	10.61 +/- 0.30	16.51 +/- 0.34
Tau_closed WT	1.53 +/- 0.02	14.04 +/- 0.58	17.83 +/- 0.88
Apo_closed WT	1.58 +/- 0.03	16.52 +/- 0.38	16.60 +/- 0.50
Sy9_closed WT	1.35 +/- 0.06	15.02 +/- 0.20	17.41 +/- 0.34
Tau_open Mutant	1.63 +/- 0.07	9.70 +/- 0.24	16.30 +/- 0.57
Tau_closed Mutant	1.64 +/- 0.14	15.20 +/- 0.47	17.54 +/- 0.31

988